atmosphere

MDPI

Article

Estimating Mean Wind Profiles Inside Realistic Urban Canopies

Huanhuan Wang [1], Eden Furtak-Cole [2] and Keith Ngan [1,3,*]

[1] School of Energy and Environment, City University of Hong Kong, Kowloon 518057, Hong Kong
[2] Division of Atmospheric Sciences, Desert Research Institute, Reno, NV 89512, USA
[3] Institute of Ocean and Earth Sciences, University of Malaya, Kuala Lumpur 50603, Malaysia
* Correspondence: keith.ngan@cityu.edu.hk

Abstract: Mean wind profiles within a unit-aspect-ratio street canyon have been estimated by solving the three-dimensional Poisson equation for a set of discrete vortex sheets. The validity of this approach, which assumes inviscid vortex dynamics away from boundaries and a small nonlinear contribution to the growth of turbulent fluctuations, is tested for a series of idealised and realistic flows. In this paper, the effects of urban geometry on accuracy are examined with neutral flow over shallow, deep, asymmetric and realistic canyons, while thermal effects are investigated for a single street canyon and both bottom cooling and heating. The estimated mean profiles of the streamwise and spanwise velocity components show good agreement with reference profiles obtained from the large-eddy simulation: the canyon-averaged errors (e.g., normalised absolute errors around 1%) are of the same order of magnitude as those for the unit-aspect-ratio street canyon. It is argued that the approach generalises to more realistic flows because strong spatial localisation of the vorticity field is preserved. This work may be applied to high-resolution modelling of winds and pollutants, for which mean wind profiles are required, and fast statistical modelling, for which physically-based estimates can serve as initial guesses or substitutes for analytical models.

Keywords: computational fluid dynamics (CFD); stratification; urban geometry; vortex dynamics; wind direction

Citation: Wang, H.; Furtak-Cole, E.; Ngan, K. Estimating Mean Wind Profiles Inside Realistic Urban Canopies. *Atmosphere* **2023**, *14*, 50. https://doi.org/10.3390/atmos14010050

Academic Editor: Daniela Cava

Received: 20 November 2022
Revised: 15 December 2022
Accepted: 21 December 2022
Published: 27 December 2022

1. Introduction

Mean wind profiles are needed for many applications. In wind engineering, a vertical profile of the horizontal wind speed is often prescribed at the inlet [1,2], while rough estimates of the wind loading are based on representative wind profiles [3]. In pollutant dispersion modelling, mean wind profiles (Since the mean vertical velocity is typically assumed to be zero, 'mean wind profiles' is used hereafter to refer to vertical profiles of the horizontal velocity components only.) lie at the heart of Gaussian plume [4] and operational dispersion [5,6] models. In atmospheric science, mean wind profiles are required to parameterise the effects of urban geometry [7].

Commonly used wind profiles are the logarithmic, for example, [8], and exponential [9] profiles. They are strictly applicable only in certain situations, for example, within the inertial sublayer [10] or where the mixing length is constant [11]. They do not apply within the urban canopy layer (UCL) [12,13], though they have been extended to the roughness sublayer [14,15]. Given the sensitivity of urban flow and dispersion to inflow boundary conditions [16,17], more accurate profiles within the canopy layer are desirable.

An alternative approach has been developed by Furtak-Cole and Ngan [18]. Applying techniques from vortex dynamics [19,20], in which the vorticity field is approximated by a piecewise constant distribution, mean wind profiles within various urban canyons were predicted with a relative error of ∼30% (with respect to a reference "truth" obtained from CFD) and a normalised absolute error of ∼1% (based on the wind speed at the roof level). The vortex method yields fast estimates of the wind profiles within the UCL (calculations are easily performed on a basic desktop computer) and improved accuracy compared

to the exponential and logarithmic profiles. Briefly, the method assumes that the mean circulation within urban canopies is strongly influenced by intense layers of vorticity (or "vortex sheets") at solid boundaries [21], which define a basis for reduced-order modelling. Although the method does not account for nonlinearity, the basis can be applied to the estimation of mean flows within urban canopies so long as the linear contribution to the growth of turbulent fluctuations is comparable to the nonlinear one. The method has been tested successfully for neutral flow, different wind directions, and relatively uniform geometries (e.g., a unit-aspect-ratio street canyon, a small building array, and a small courtyard).

The applicability of the vortex method to real cities is unclear. In most cities, the aspect ratio ($AR \equiv H/W$ or the ratio of building height to street width) may deviate significantly from unity, for example, [22,23]. Since multiple vortices may exist for two-dimensional street canyons with $AR \gtrsim 1.5$, for example, [24,25], the method developed for $AR \sim 1$ and a single coherent vortex may need to be modified for deep canyons. Similar caveats apply to shallower canyons, for example, flow in the isolated roughness ($AR \lesssim 0.3$) and wake interference ($0.3 \lesssim AR \lesssim 0.65$) regimes, where the flow is less dominated by the canyon vortex, and inhomogeneous domains, which cannot be described by a single number like the aspect ratio. Furthermore, a method based on approximating the vorticity may not be well-suited to stratified flow, which cannot be described in terms of a vortical component only. Assessing the applicability of the vortex method to stratified flow is necessary because important phenomena like the urban heat island, for example, [26,27] and pollutant trapping by temperature inversions, for example, [28,29] cannot be simulated using neutral flow.

This study investigates the applicability of the vortex method to a series of progressively more realistic configurations. The key scientific questions are: (i) does the method need to be modified to account for geometric or thermal effects? (ii) is the accuracy of the estimated wind profiles maintained for realistic urban canopies? (iii) what are the physical reasons why the method is able to extend to a more realistic flow? The vortex method and the CFD configurations are reviewed in Section 2. The vortex method is applied to neutral flow over domains of varying geometrical complexity and stratified flow with bottom heating or cooling. Results for different geometries and stratifications are presented in Sections 3 and 4, respectively. The extent to which the method generalises to realistic canopies is discussed in Section 5. The benefits and limitations of the method are summarised in Section 6.

2. Methodology

2.1. Vortex Method

The vortex method seeks to define a set of basis functions that can be used to estimate spatially averaged wind profiles. The basis functions are obtained from a simplified set of equations rather than the governing equations (for neutral, inviscid flow). More precisely, the basis functions are obtained by solving the Poisson equation for an approximate vorticity distribution. The original equations are recovered if the original vorticity distribution is used, though there is no dimensional reduction to be had in this case; however, if the vorticity exhibits strong spatial localisation, attention can be focused on a piecewise constant distribution in which the vorticity components have prescribed values in certain regions and are zero elsewhere, leading to potentially large computational savings. Although a piecewise-constant vorticity distribution may appear to be a severe approximation, the same idea underlies standard models in vortex dynamics such as vortex patches or ellipsoids [19], numerical techniques such as contour dynamics [30], and reduced-eddy models in geophysics [31]: the equations of motion are not violated because closed vortex lines may be defined within a uniform-vorticity region. Since the real vorticity distribution is continuous, the accuracy of the approximation depends on the degree of spatial localisation. For flow within urban canopies, one may expect the magnitude of the

velocity gradients and vorticity to be large near solid boundaries and the roof level (see Ngan and Lo [21] for confirmation in the case of a single street canyon).

By definition, the contribution of each basis function should be independent of the others. Strictly speaking, this implies that nonlinear effects should be small so that the nonlinear contribution to turbulent fluctuations is small compared to the linear one. In practice, a linear basis may constitute a useful approximation for a fully turbulent flow so long as the linear contribution is sufficiently large. For flow over a single street canyon, the growth of fluctuations within a street canyon is well-predicted by the linearised dynamics [32]. For a real urban canyon, the linear term of the turbulent kinetic energy (TKE) budget equation may be comparable to or larger than the nonlinear one near the roof level [33]; similar results have been obtained for a single street canyon (not shown).

For the basis to be applied to the estimation of mean wind profiles, calibration is required, as with statistical or machine learning approaches [34–36], which require training data (i.e., measurements or baseline numerical simulations) to derive statistical coefficients. In this study, calibration constants, namely factors that depend on the geometry and the mean flow or vortex sheet strength, are obtained for a specific geometry and wind direction. The usefulness of the method hinges on whether these calibration constants can be applied to other cases (e.g., wind directions).

The procedure outlined above is now summarised. The formulation for unit-aspect-ratio street canyons [18] is generalised by allowing for an arbitrary number of vortex sheets and vorticity components. Mathematical details may be found in Appendix A.

1. *Definition of the vortex sheets.* Since strong velocity gradients occur near solid walls with no-slip boundary conditions, vorticity components are strongly localised near them. The vorticity field is, therefore, decomposed into a set of fixed, uniform vortex sheets located at the top ($\Re^t$, the highest building height), bottom ($\Re^b$, street level) or side ($\Re^s$) walls; for uneven geometries, intermediate vortex sheets ($\Re^i$) may be located on top of buildings. Figure 1 shows schematic illustrations of the vortex sheets for the domains considered in this study. In theory, all three vorticity components may be included for each vortex sheet; however, the predictive value of the method is lower if more basis functions are included as more calibration data are required. A subset of vorticity components and vortex sheets is, therefore, considered for the cases analysed in Section 3. Hereafter, the shorthand term 'vorticity sheet' refers to the combination of a vortex sheet location and vorticity component.
2. *Solution of Poisson equation.* Velocity basis functions, $\langle v_i^{j,\omega_k} \rangle$, are obtained for vortex sheet j with vorticity component ω_k and unit vorticity magnitude by solving a three-dimensional Poisson Equation (A4) and horizontally averaging the Green's function (or numerical solution). The Green's function encapsulates the effect of the building geometry on the flow induced by a specific vorticity sheet. The Poisson equation is solved using a geometric-algebraic multi-grid solver and a free-slip boundary condition on solid surfaces; the boundary conditions are otherwise identical to the CFD model (Section 2.2), as is the computational mesh (Section 2.3).
3. *Synthesis.* Mean wind profiles in the canyon interior are obtained by linear superposition, i.e., by summing over vortex sheets and vorticity components:

$$\langle u_i \rangle(z) = \sum_{j,\omega_k} \alpha^{j,\omega_k} \langle v_i^{j,\omega_k} \rangle(z), \tag{1}$$

where $i = \{x, y\}$ and the α^{j,ω_k} may be interpreted as weights that represent the strength of each vorticity sheet. The angle brackets denote the horizontal (fluid-only) average over the computational domain. The entire set of vorticity sheets (i.e., three vorticity components at each solid surface) could be included; however, this necessitates additional training data (see the calibration step below). To avoid the possibility of overdetermining or biasing the results, reduced sets are considered. They can be determined through an objective procedure (see Appendix B).

4. *Calibration.* The weights are obtained by calibrating the basis functions against reference velocity data. The α^{j,ω_k} are taken to be proportional to the strength of each vorticity sheet, i.e.,

$$\alpha^{j,\omega_k} \equiv C^{j,\omega_k}\gamma^{j,\omega_k} \tag{2}$$

where γ^{j,ω_k} is the circulation of the vorticity sheet. Assuming that the structure of the vorticity sheets is unchanged with the wind direction, θ, the C^{j,ω_k} depends on the geometry only, i.e., they are essentially geometric constants; this assumption may be tested by applying the C^{j,ω_k} to other wind directions. Minimising the residual between the true profile, $\left\langle u_i^{(t)} \right\rangle$, and the estimated profile at a specific θ,

$$r = \int_{z_b}^{z_t} \left(\sum_{j,\omega_k} \alpha^{j,\omega_k} \left\langle v_i^{j,\omega_k} \right\rangle - \left\langle u_i^{(t)} \right\rangle \right)^2 dz, \tag{3}$$

yields the geometric constants. The integral is taken over the interval, $[z_b, z_t]$, where z_b lies above the viscous boundary layer at the bottom, and z_t is the (mean) canopy height. Unless otherwise stated, the geometric constants correspond to the wind direction $\theta = 45°$. The local tangential velocity, $\langle u_i \rangle_s$, is used to calculate γ^{j,ω_k}. Note that γ^{j,ω_k} but not C^{j,ω_k} is a function of θ.

5. *Matching.* Since inviscid vortex dynamics are assumed, the interior vortex solution must be matched to the no-slip boundary condition at the ground. A logarithmic profile is introduced between the ground and the top of the log layer, i.e., z_b, by defining the friction velocity from the log-law prediction. By construction, the log profile exerts no influence on the predicted profile in the interior, $z > z_b$. For typical urban canyons, the streamwise velocity profile is not logarithmic near the ground: the log profile is chosen simply for convenience.

The implementation differs slightly from [18]. First, a more objective procedure is adopted for the determination of the profile near the ground. In the present study, z_{ref} is defined by restricting it to the top of the log layer, i.e., $y^+ \sim 200$, for example, [37], where y^+ is the distance in normalised wall units. Compared to the previous choice for a single street canyon, $z_{\text{ref}} = 0.25H$, the width of the log layer (with roughness length $z_0 = 0.1$ m) decreases to $0.08H$: thus, the vortex prediction covers a wider region. Second, the tangential velocity at the vortex sheets, $\langle u_i \rangle$, is obtained by direct averaging of the reference velocity data rather than extrapolation from the centre.

2.2. CFD Configurations

Although this study is not primarily concerned with the analysis of CFD simulations, CFD data are required to calibrate the vortex method and define reference profiles. Both neutral and stratified simulations are considered. The governing equations in the latter case are given by the non-hydrostatic Boussinesq equations; in the neutral case, all temperature terms are dropped.

Neutral simulations for the idealised and realistic canyons were performed using OpenFOAM, a finite-volume library for partial differential equations [38,39], improved delayed detached eddy simulation (IDDES) [40] and implicit filtering. IDDES is used instead of a more computationally efficient method based on the Reynolds-Averaged Navier–Stokes equations because the calibration and testing require accurate reference data; it is well-established that RANS is less accurate than LES and LES-like methods [41]. The configuration of the neutral simulations follows [18]. Crank–Nicolson time-stepping is combined with a Gauss scheme for advection and second-order Gauss linear upwinding for the velocity divergence. There are periodic boundary conditions at the horizontal and Dirichlet at the top. The Spalding [42] wall function (implemented in OpenFOAM as *nutUSpaldingWallFunction*) is applied to solid surfaces. It prescribes the turbulent viscosity

as a function of the wall-normal distance by correcting the shear stress at the wall. Although the small-scale vorticity field depends on the mesh details and wall function, the mean velocity profiles show limited sensitivity (Appendix C).

Stratified simulations for a unit-aspect-ratio street canyon were conducted with the Parallelized Large-eddy Simulation Model, PALM [43], with implicit filtering and a 1.5-order subgrid scheme [44,45]. PALM has been used in many studies of urban boundary layers [46–48], including stratified ones [49]. The configuration of the stratified simulations follows Wang and Ngan [50]. The velocity boundary conditions are identical to the neutral case; a Prandtl layer with $z_0 = 0.1$ m is used for the wall function. With respect to the temperature, a fixed value $T_0 = 300$ K is prescribed at the inlet, while there is a radiation boundary condition at the outlet. Following [51–53], the heating is specified by fixing the temperature of the bottom boundary, i.e., the ground temperature is specified as $T_b - T_0 \equiv \Delta T$, where ΔT denotes the heating or cooling.

In all cases, the mean flow is forced by external forcing. For the neutral simulations in OpenFOAM, a wind speed of $3\,\mathrm{m\,s^{-1}}$ is specified at the upper lid; for the stratified simulations in PALM, a constant external pressure gradient of -0.0006 Pa m^{-1} is applied. The forcing is rotated to vary the wind direction. The default time step $\Delta t \sim 0.1$ s, and the domain-averaged Courant number is always less than unity. After an initial spin-up of 4000 s, the data are averaged over 1000 s. All of the results shown below are time-averaged (indicated by the overbar).

2.3. Computational Domains

A wide range of urban geometries is investigated. Schematic illustrations of the computational domains are shown in Figure 1, namely shallow or deep (Figure 1a), step-up (Figure 1b) and step-down (Figure 1c) canyons, and realistic neighbourhoods (Figure 1d,e) canyons. For the idealised canyons (Figure 1a–c), the streamwise (x) direction ($\theta = 0°$) is perpendicular to the canyon axis, while the spanwise (y) direction ($\theta = 90°$) is parallel to it. The canyons have width W and length L, the buildings are of width $W/2$, and the domain dimensions are listed in Table 1. For realistic geometries, the horizontal dimensions and building heights vary. For the homogeneous neighbourhood (Figure 1d), the mean building height is 41 m, the standard deviation is 4.5 m and $AR \sim 1 - 3$; for the heterogeneous neighbourhood (Figure 1e), the mean building height is 48 m, the standard deviation is 28 m and the tallest building is 100 m. In both cases, a buffer region of width 40 m is applied around the periphery of the domain. The domain dimensions and building heights are summarised in Table 1.

An isotropic grid spacing $\Delta = 1$ m is used away from the walls for the OpenFOAM simulations and throughout the computational domain for the PALM simulations. The resolution is consistent with recent urban CFD studies, for example, [50]. For the idealised canyons only, mesh refinement is applied in the immediate vicinity of the walls only by introducing an additional mesh layer so that the finest horizontal resolution is $\Delta = 0.5$ m. Grid convergence tests are described in Appendix D.

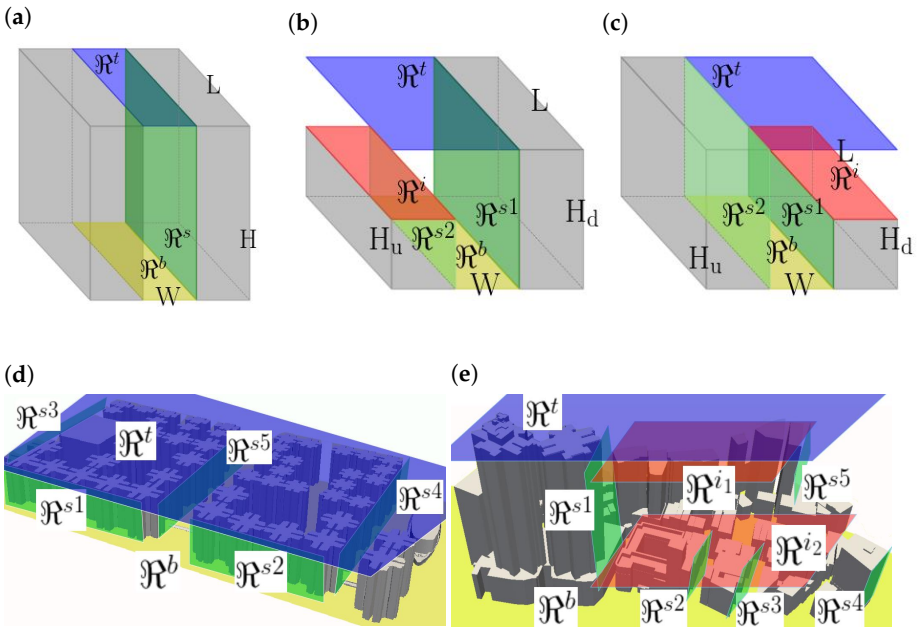

Figure 1. Urban geometries and vortex sheets (**a**) shallow or deep canyon; (**b**) step-up canyon; (**c**) step-down canyon; (**d**) homogeneous neighbourhood (Whampoa, Hong Kong); (**e**) heterogeneous neighbourhood (Central, Hong Kong). The vortex sheets are indicated in colour: roof level, $\Re^t$ (violet); ground level, $\Re^b$ (yellow); intermediate, $\Re^i$ (red); sidewall, $\Re^s$ (green). There are several intermediate and sidewall vortex sheets, denoted as $\Re^{i_k}$ and $\Re^{s_k}$, for the asymmetric and realistic canyons. Computational domain parameters are described in Table 1.

Table 1. Computational domain parameters. L_x, L_y, L_z denote the domain dimensions; H, W, L are the building dimensions. For more complicated domains, H_u is the height of upstream building, H_d is the height of the downstream building and H_{avg} is the mean building height.

Canyon	AR	L_x	L_y	L_z	W	H	L	Illustration
Shallow	0.25	$5H$	$3H$	$5H$	200 m	50 m	150 m	Figure 1a
	0.5	$3H$	$3H$	$5H$	100 m	50 m	150 m	Figure 1a
Deep	1	$2W$	$3W$	$5H$	50 m	50 m	150 m	Figure 1a
	3	$2W$	$3W$	$5H$	50 m	150 m	150 m	Figure 1a
Step-up	-	$2W$	$3W$	$5H_d$	50 m	H_u: 50 m; H_d: 100 m	150 m	Figure 1b
Step-down	-	$2W$	$3W$	$5H_u$	50 m	H_u: 100 m; H_d: 50 m	150 m	Figure 1c
Whampoa	∼1.4	480 m	480 m	200 m	-	H_{avg}: 41.4 m	-	Figure 1d
Central	∼2	260 m	140 m	500 m	-	H_{avg}: 48 m	-	Figure 1e

2.4. Validation

The OpenFOAM configuration for neutral flow (Section 2.2) is validated against the wind tunnel data of [54], which correspond to measurements of the flow over a set of street canyons with $AR = 1$. As in recent urban CFD studies, for example, [55,56], the validation is performed using an idealised geometry rather than a realistic one because wind-tunnel or in situ measurement data are not available. Since the mean wind speed and Reynolds numbers for idealised and realistic geometries are similar (see Section 2.2 and Table 1), one may expect the model's overall performance to be broadly similar in the latter case. Vertical profiles of the mean streamwise velocity and TKE evaluated at different streamwise locations show good agreement between IDDES and the wind-tunnel data

(Figure 2). Statistical performance measures [57] indicate a successful validation: fractional bias $FB \sim 0.02$–0.05, the normalised mean square error $NMSE \sim 0.03$–0.06, fraction of data $FAC2 \sim 0.9$ and correlation coefficient $R \sim 1$. Given that the vortex method is concerned with mean velocity profiles rather than fine-scale turbulence statistics, we conclude that the neutral-flow simulations with OpenFOAM can serve as a baseline truth against which the vortex method can be tested.

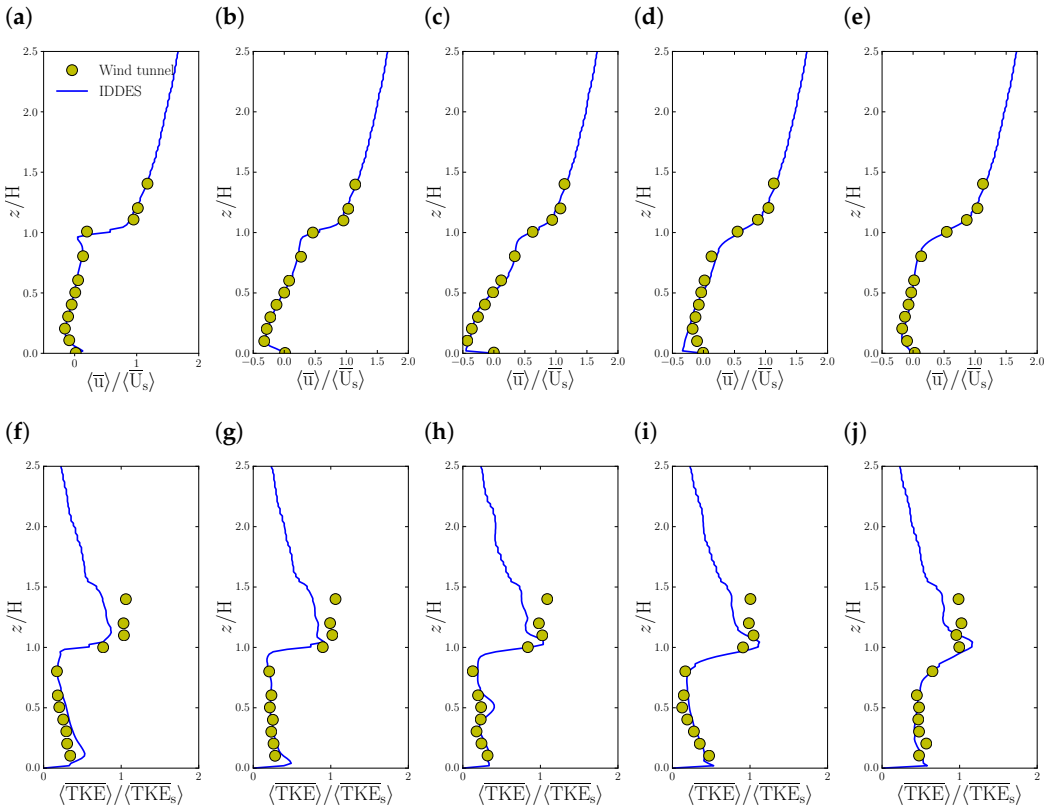

Figure 2. Validation of the IDDES model (OpenFOAM) for neutral flow over a 2-D street canyon. Normalised mean streamwise velocity and TKE validation of IDDES (solid line) against wind tunnel experiment [54] (filled circles) at (**a**,**f**) $x/W = -0.4$; (**b**,**g**) $x/W = -0.25$; (**c**,**h**) $x/W = 0$; (**d**,**i**) $x/W = 0.25$; (**e**,**j**) $x/W = 0.4$. Reference values for the streamwise velocity and TKE, $\langle \overline{U_s} \rangle$ and $\langle \overline{TKE_s} \rangle$, represent averages of the IDDES data over the shear layer, $1 \leq z/H \leq 1.5$.

The PALM configuration for stratified flow over a street canyon is validated against wind-tunnel measurements of flow over a regular array of cubic buildings [58]. To ensure that the plan and frontal area ratios match the experiment, the aspect ratios of the nominal canyon units along the x and y directions are 1 and 0.5, respectively. The agreement between the current LES results and the experimental data is generally good (Figure 3). For the most unstable case, the fractional bias $FB \sim 0.02$–0.06, the normalised mean square error $NMSE \sim 0.04$–0.08 and fraction of data $FAC2 \sim 0.96$. The validation confirms that PALM is able to simulate credible reference profiles for stable and unstable stratification.

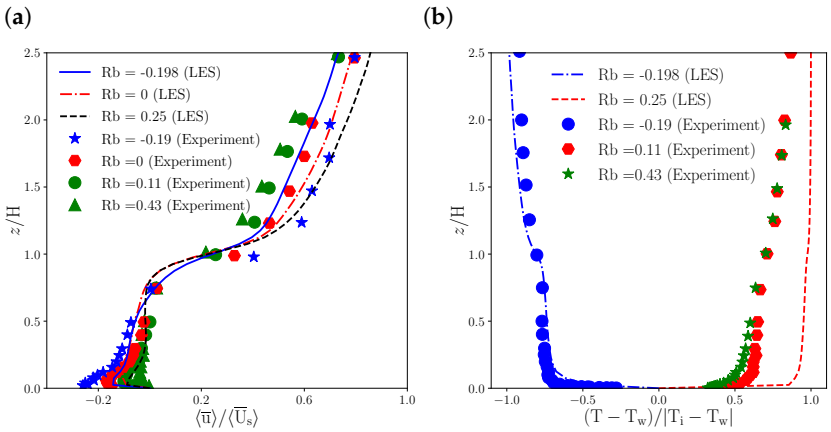

Figure 3. Validation of the LES model for stratified flow over a regular array against the wind-tunnel data of Uehara et al. [58]: (**a**) streamwise velocity; (**b**) temperature. The bulk Richardson number Rb is defined in Equation (14).

2.5. Errors

From the predicted and true profiles, $\langle u_i^{(p)} \rangle$ and $\langle u_i^{(t)} \rangle$ respectively, the absolute and relative errors are defined by,

$$\varepsilon_a = \frac{1}{U_{\text{ref}} H} \left(\int_{z_1}^{z_2} \left(\langle u_i^{(p)} \rangle - \langle u_i^{(t)} \rangle \right)^2 dz \right)^{1/2}, \tag{4a}$$

$$\varepsilon_r = \varepsilon_a \left(\frac{1}{U_{\text{ref}} H} \left(\int_{z_1}^{z_2} \langle u_i^{(t)} \rangle^2 dz \right)^{1/2} \right)^{-1}. \tag{4b}$$

For convenience, $\varepsilon_a, \varepsilon_r$ refer to $(z_1, z_2) = (0, H)$ and $\varepsilon_a', \varepsilon_r'$ refer to $(z_1, z_2) = (z_b, H)$, where $z_b = 0.08H$ is the top of the log layer. U_{ref} is a reference velocity, the streamwise velocity at $z/H = 1$, where the unnormalised streamwise errors are maximised. Although the relative error is independent of H and U_{ref}, ε_r can be anomalously large when the mean flow is weak and the denominator (i.e., $|\langle u_i^{(t)} \rangle|$) is small. The reference velocity is defined using the roof-level value rather than a canyon average because the latter is very small: for $AR = 3$, the canyon average, U_{avg}, is approximately three orders of magnitude smaller than U_{ref}. Both ε_a and ε_r are considered because neither definition is appropriate for all situations. For example, small absolute errors yield large relative errors when $u^{(t)}$ is close to zero.

3. Geometric Effects

In this section, the applicability of the vortex method to neutral flow over different building geometries is investigated.

3.1. Shallow Canyons

The accuracy of the vortex method may depend on the aspect ratio because the assumptions underlying the vortex method may not be satisfied for certain flow regimes. Hence shallow canyons with $AR = 0.25$ and 0.5, belonging to the isolated roughness (IR) and wake interference (WI) regimes [59,60], respectively, are examined. For convenience, results for $AR = 1$ or skimming flow (SF) are also shown.

As AR increases, the canyon-wide circulation (Figure 4a–c) becomes increasingly dominated by the strong central vortex (Figure 4d–f). The vorticity is strongly localised at the roof and bottom levels for all three regimes; however, the normalised turbulent kinetic energy (TKE) within the canopy increases for the shallower canyons (panels Figure 4g–i).

The mean horizontal velocity components can be estimated with the same vorticity sheets (Figure 1a) as for $AR = 1$ see [18] (Figure 3):

$$u_x : \Omega^{shallow} \equiv \{(\Re^b, \omega_y), (\Re^t, \omega_y)\} \tag{5a}$$

$$u_y : \Omega^{shallow} \equiv \{(\Re^s, \omega_z)\}. \tag{5b}$$

This is a reasonable assumption because the structure of the mean flow and the localisation of the vorticity sheets are similar for $AR \lesssim 1$. By symmetry, only a single sidewall vortex sheet is required. Each vorticity sheet extends along the full length of the canyon in the spanwise direction. Strictly speaking, the contribution of $\Re^s$ to u_x could be included; however, it is very small (see Appendix B for an analysis for $AR = 3$).

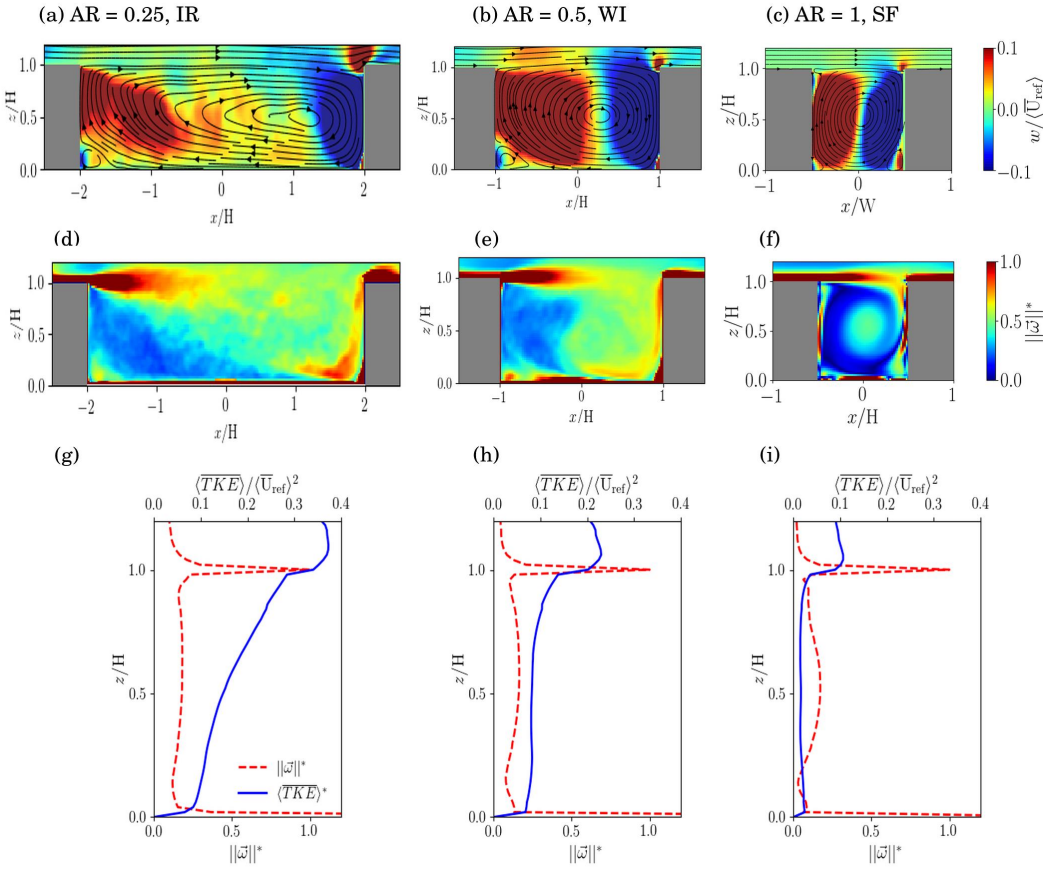

Figure 4. Flow structures in the $x-z$ plane for uniform street canyons with a mean flow perpendicular to the canyon axis ($\theta = 0°$): (**left**) $AR = 0.25$; (**middle**) $AR = 0.5$; (**right**) $AR = 1$. (**a–c**) Temporally and spatially averaged streamlines; vertical velocities are plotted in colour; (**d–f**) spatially averaged vorticity magnitude normalised by the maximum value, $||\vec{\omega}||^*$; (**g–i**) vertical profiles of the TKE and $||\vec{\omega}||^*$. The TKE is normalised using $\langle \bar{U}_{\text{ref}} \rangle$, the IDDES streamwise velocity at $z/H = 1$.

The estimated and true wind profiles for $\theta = 0°$ are compared in Figure 5. For all three regimes, there is very good agreement in the interior, but large deviations at the bottom, where the log profile is applied. The canyon-averaged relative errors satisfy $\varepsilon_r \sim 0.30$ and 0.13 for u_x and u_y, respectively, while $\varepsilon_a \sim 0.017$ for the absolute errors. Similar results are obtained for other $\theta \in [0°, 90°]$ except for u_y at $\theta = 90°$. The reasons for this are discussed in Section 3.2.

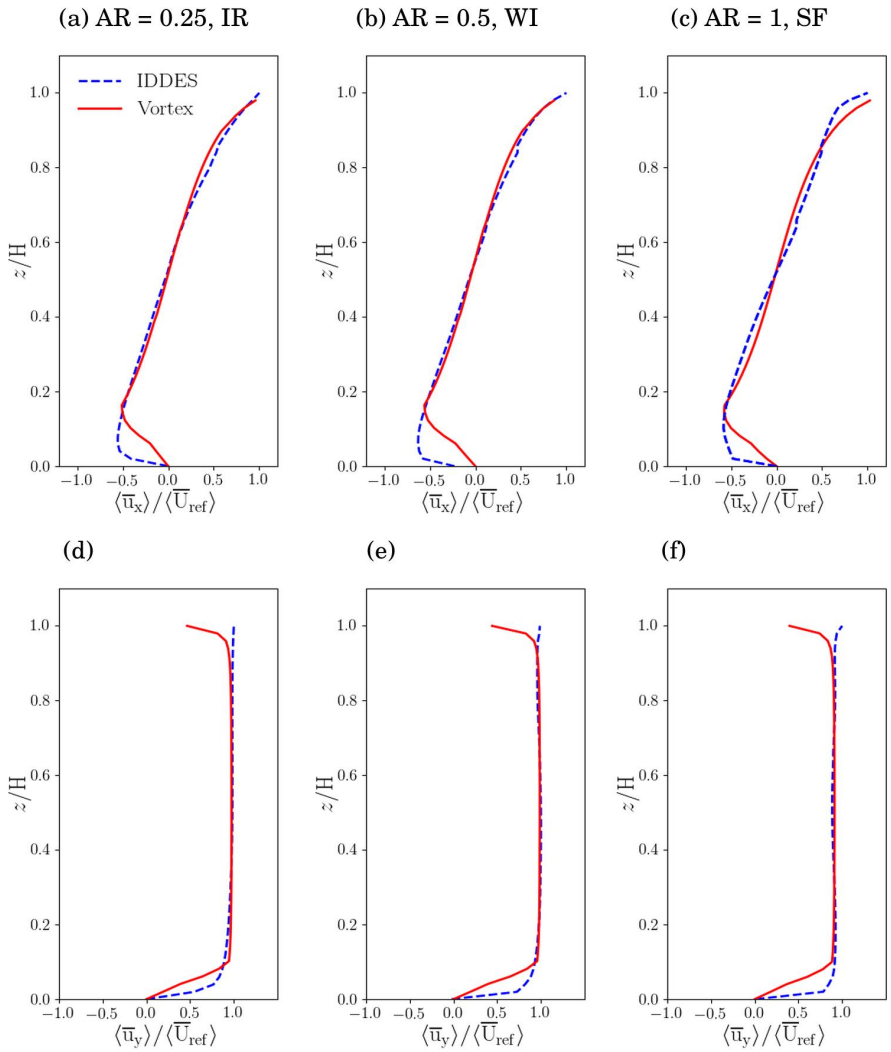

Figure 5. Vertical profiles of normalised velocities for $AR \leq 1$ and $\theta = 0°$. Estimated (solid lines) and IDDES (dashed lines) profiles are compared for: (**a**,**d**) $AR = 0.25$; (**b**,**e**) $AR = 0.5$; (**c**,**f**) $AR = 1$. Streamwise (**top**) and spanwise (**bottom**) velocities are normalised by $\langle \bar{U}_{\mathrm{ref}} \rangle$, the IDDES streamwise velocity at z/H=1. Henceforth this definition of $\langle \bar{U}_{\mathrm{ref}} \rangle$ is used for all vertical profiles.

The estimates are not strongly affected by the increase in the normalised TKE for the shallower canyons. The relative error actually increases slightly from the IR to SF regimes, though there is a smaller decrease in the absolute error.

3.2. Deep Canyons

Deep canyons with $AR > 1$ are commonplace in cities with tall skyscrapers. Since multiple vortices may occur inside them [24], accuracy may be affected. A deep canyon with $AR = 3$ is examined below.

In agreement with previous studies [61,62], the large vortex of the shallow canyons is replaced by a pair of vortices (Figure 6a). The spanwise vorticity is maximised at the roof level, with smaller contributions from the sidewalls and bottom (Figure 6b). The vorticity magnitude has a similar appearance (not shown), but a signed vorticity component is more appropriate for a flow with multiple vortices. Despite the appearance of a second vortex, the vorticity in the bottom half of the canyon is relatively weak. The normalised TKE is also small, away from the roof level.

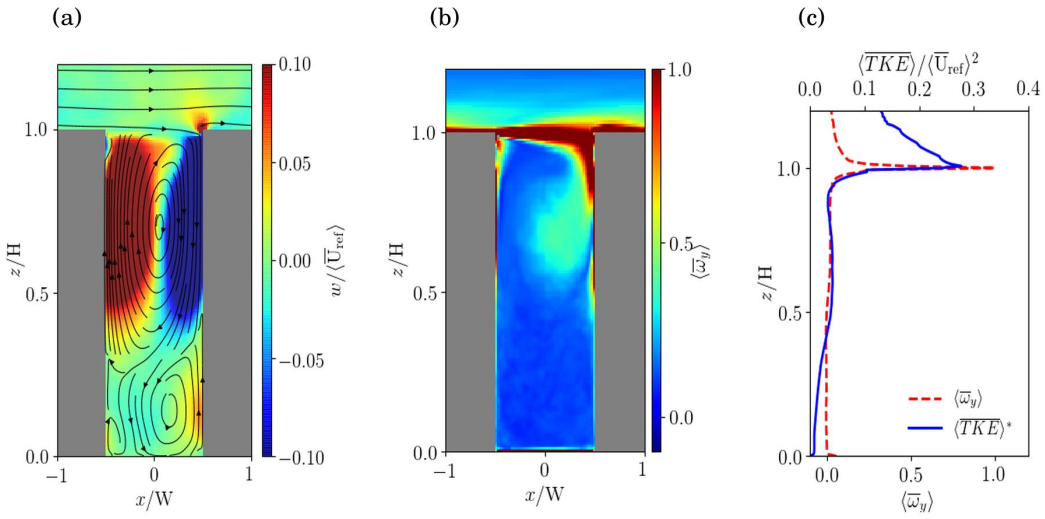

Figure 6. Flow structures for a deep canyon with $AR = 3$ and $\theta = 0°$. (**a**) Temporally and spatially averaged streamlines; (**b**) spanwise vorticity; (**c**) vertical profiles of the TKE and spanwise vorticity. As in Figure 4, the streamlines and vorticity field are averaged in the spanwise direction.

From the appearance of the TKE and vorticity profiles, vortex sheets can be defined similarly to the shallow canyons, i.e., by using $\Omega^{deep} \equiv \Omega^{shallow}$ (Figure 1a). To allow for a fair assessment of the method, the geometric constants for $\theta = 45°$ are used for other wind directions, even though the vorticity structure may change. Mean wind profiles are plotted for different θ in Figure 7: for u_x, the inflection point near the middle of the canyon is not captured; for u_y, agreement tends to be better, but there are large relative errors for $\theta = 90°$. The agreement at 90° for both u_x and u_y improves when the geometric constants are calculated at 90° rather than 45°, i.e., ε_r for u_x decreases from 66% to 30%. Given that the flow structure for $\theta = 90°$, namely a channel-like flow, differs qualitatively from other wind directions, this is unsurprising. Nevertheless, a useful approximation to the actual u_y profile is still obtained using the "wrong" vortex sheets and geometric constants: the monotonic structure is preserved, and there is still residual skill. The canyon-averaged errors for different θ are listed in Appendix F, Table A6.

At $\theta = 45°$, the accuracy decreases compared to the shallow canyons (Figure 5) since the inflection point near $z/H = 0.5$ in the u_x profile is missed. This can be attributed to the neglect of the second vortex, which appears in the lower half of the canyon. A potential solution is discussed in Section 5.

The dependence of the errors on the aspect ratio is summarised in Figure 8. At 45° (panel a), the relative errors are maximised in the WI regime, which is where the interaction between turbulent wakes is strongest. There is similar behaviour for u_x but not u_y at 90° (panel b); this discrepancy can be attributed to the application of the geometric constants for 45° to the special case of channel flow at 90°. When the calibration is also done at 90°, the u_y error is also maximised in the WI regime (not shown).

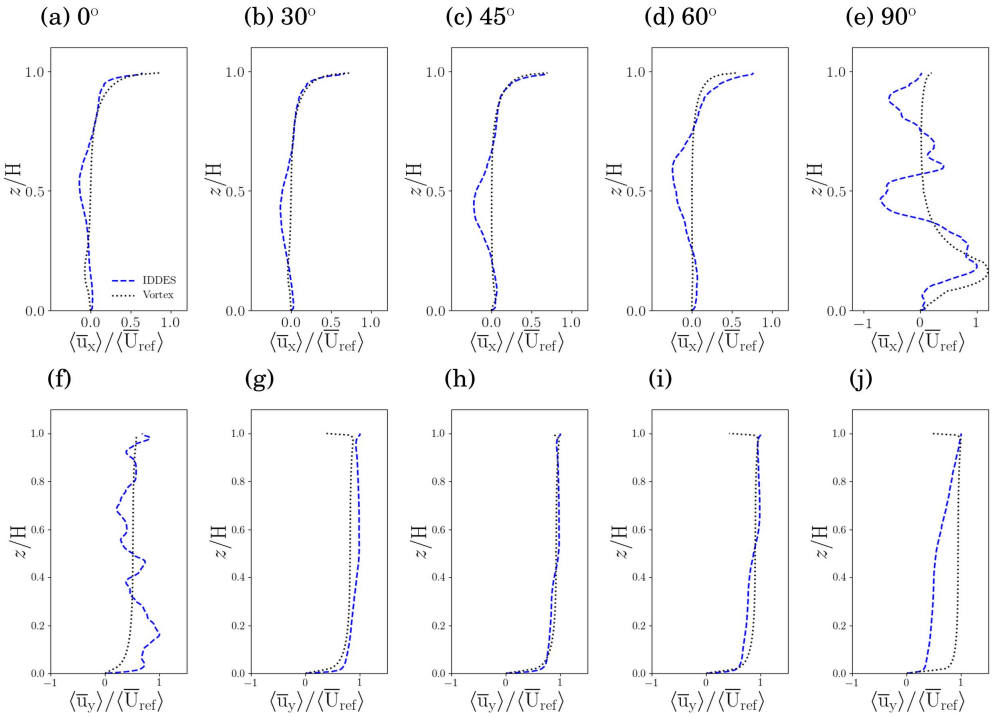

Figure 7. Vertical profiles of normalised velocities for the deep canyon ($AR = 3$) and various θ. Mean streamwise (**top**) and spanwise (**bottom**) profiles are shown for the vortex method (dotted black line) and IDDES (dashed blue line). (**a**,**f**) $\theta = 0°$; (**b**,**g**) $\theta = 30°$; (**c**,**h**) $\theta = 45°$; (**d**,**i**) $\theta = 60°$; (**e**,**j**) $\theta = 90°$. The mean streamwise velocity at $z/H = 1$ is used for the normalisation.

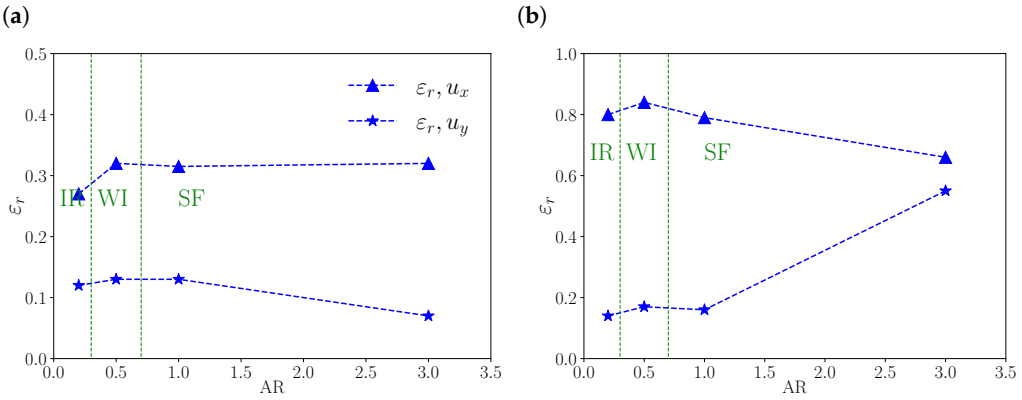

Figure 8. Variation of the canyon-averaged relative errors with AR at (**a**) $\theta = 45°$; (**b**) $\theta = 90°$.

3.3. Asymmetric Canyons

By contrast with the idealised geometries of Sections 3.1 and 3.2, street canyons in real cities may not be formed by buildings of identical height. An asymmetric street canyon (Figure 1b,c) is formed by upwind and downwind buildings of unequal height, H_u and H_d. A key parameter characterising this geometry is the building ratio,

$$BR \equiv H_d / H_u. \tag{6}$$

A step-up canyon corresponds to $BR > 1$ (Figure 1b) and a step-down canyon to $BR < 1$ (Figure 1c).

We consider several step-up and step-down cases (Table 2). For $BR > 1$, $H_d \equiv W$ is fixed and H_u varied, while for $BR < 1$, $H_u \equiv W$ is fixed and H_d varied. Since the boundary conditions are identical to those for the shallow and deep canyons, flow over an infinite array of asymmetric canyons is simulated. Despite the superficial resemblance, the

configurations are rather different from isolated step-up and step-down canyons [63,64]. Neither isolated asymmetric canyons nor asymmetric infinite arrays are entirely representative of typical urban neighbourhoods, but periodic boundary conditions are adopted here to minimise the computational cost and to facilitate comparison with the shallow and deep canyons.

Table 2. Step-up and step-down canyon parameters.

Canyon	BR	W	H_u	H_d	L
Step-up	4	50 m	25 m	100 m	150 m
	2	50 m	50 m	100 m	150 m
	1.33	50 m	75 m	100 m	150 m
Step-down	0.75	50 m	100 m	75 m	150 m
	0.5	50 m	100 m	50 m	150 m
	0.25	50 m	100 m	25 m	150 m

Flow structures for step-up ($BR = 2$) and step-down ($BR = 0.5$) canyons are illustrated in Figure 9. In both cases, two vortices appear inside the canyon. For the step-up canyon (Figure 9a–c), the primary vortex is located between the walls of the two buildings ($-0.5 < x/W < 0.5$), while a secondary vortex is located above the upwind building. For the step-down canyon (Figure 9d–f), the upper vortex spans the entire width of the canyon ($-0.5 < x/W < 1.0$), while the lower vortex is confined between the buildings ($-0.5 < x/W < 0.5$). The effect of the lower building on the TKE and vorticity profiles is more obvious for the step-down canyon, presumably because the flow within the step-up canyon is dominated by the downwind wall. Aside from the strong vorticity gradient introduced by the lower building of the step-down canyon, the spatial localisation of the vorticity and TKE do not differ significantly from the deep canyon (Figure 6).

The choice of vortex sheets (Figures 4b,c) follows the structure of the vorticity field. In addition to the intense layers of vorticity at the walls, there is a new layer above the lower building. This, therefore, suggests the following arrangement of vorticity sheets (Figure 1b,c),

$$u_x : \Omega^{step-up} \equiv \{(\Re^b, \omega_y),\ (\Re^{i_u}, \omega_y), (\Re^t, \omega_y)\}, \tag{7a}$$

$$u_x : \Omega^{step-down} \equiv \{(\Re^b, \omega_y),\ (\Re^{i_d}, \omega_y), (\Re^t, \omega_y)\}, \tag{7b}$$

$$u_y : \Omega^{step-up}, \Omega^{step-down} \equiv \{(\Re^{s_1}, \omega_z),\ (\Re^{s_2}, \omega_z)\}, \tag{7c}$$

where $\Re^{i_u}$ and $\Re^{i_d}$ are intermediate vortex sheets located on top of the upwind and downwind buildings, respectively, and $\Re^{s_1}$, $\Re^{s_2}$ are the sidewall vortex sheets. $\Re^{i_u}$ and $\Re^{i_d}$ are restricted to the rooftops because, by contrast with $\Re^t$, intense vorticity does not extend across the canyon.

The wind profiles for streamwise (u_x) and spanwise (u_y) velocities are shown in Figure 10. The results are averaged over $-1 < x/W < 0.5$ for the step-up cases and $-0.5 < x/W < 1$ for the step-down cases. The true u_x step-up profiles for $BR \in [1.33, 4]$ resemble that for the deep canyon, indicating that the influence of the lower building is weak, but the true step-down profiles for $BR \in [0.25, 0.75]$ show an inflection point around the roof level of the lower building. The relative errors for u_x increase from $BR < 1$ to $BR > 1$, while those for u_y are approximately constant. For the cases with an inflection point in u_x, the accuracy of the estimate is compromised (e.g., $\varepsilon_r \sim 0.9$) when the intermediate vortex sheet is excluded. Although the profiles are more complicated than those for the shallow and deep canyons, the agreement is generally quite good, despite the nonlinearity of the profiles. The dependence of the errors on BR is depicted in Appendix E, Figure A6.

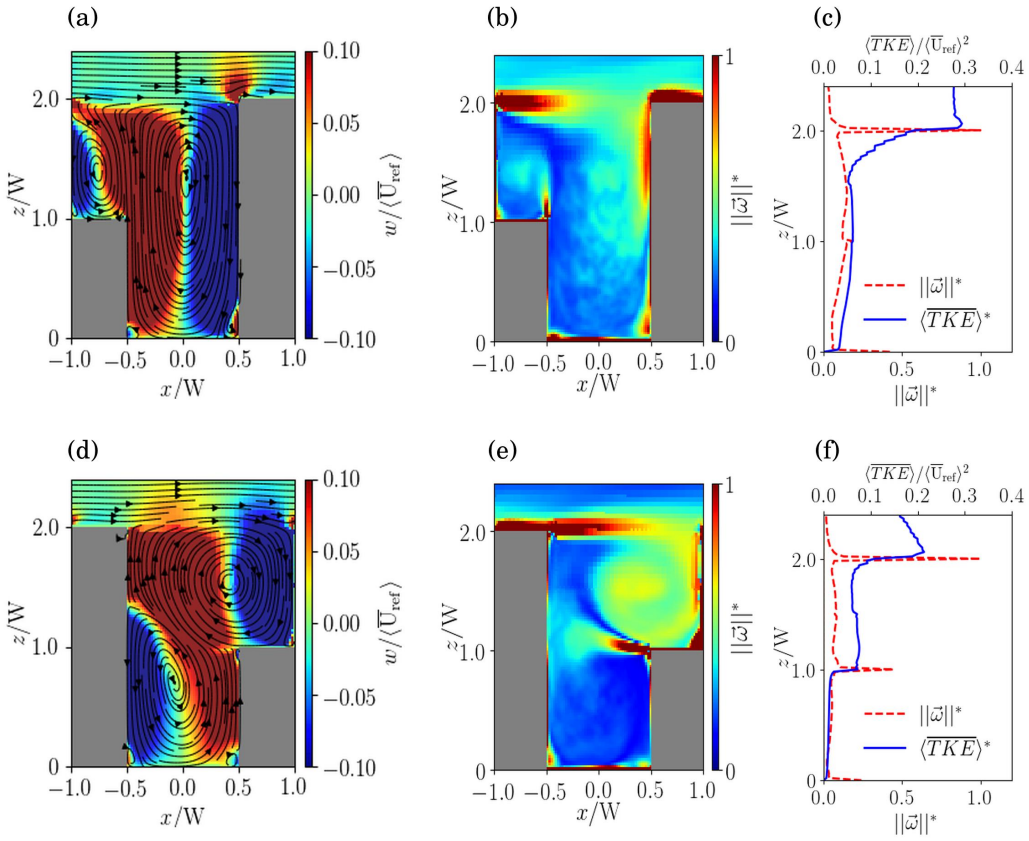

Figure 9. As in Figure 4 but for asymmetric canyons. (**Top**) step-up canyon ($BR = 2$); (**bottom**) step-down canyon ($BR = 0.5$). (**a**,**d**) Temporally and spatially averaged streamlines; (**b**,**e**) spatially averaged vorticity magnitude; (**c**,**f**) vertical profiles of the normalised TKE and vorticity magnitude.

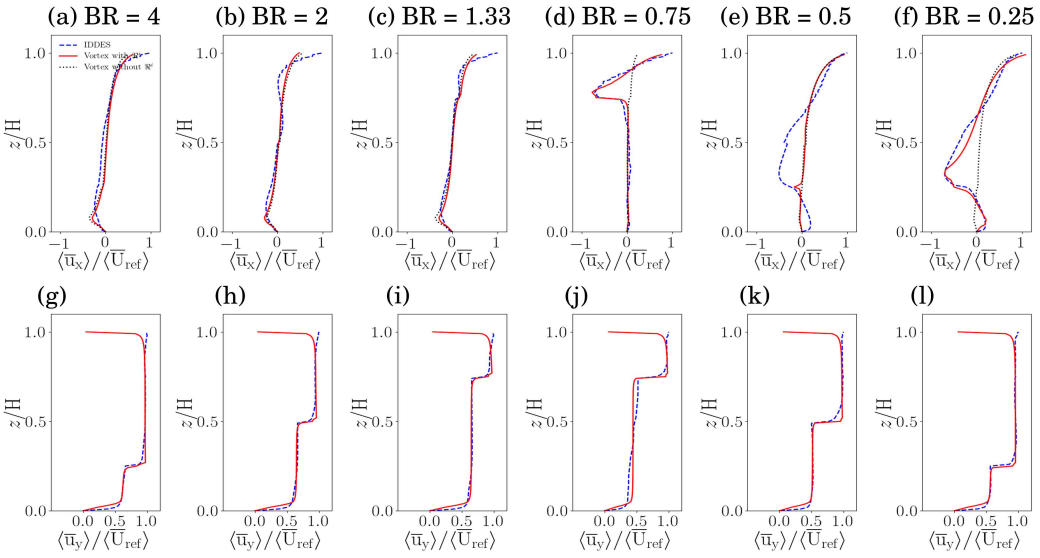

Figure 10. Vertical profiles of normalised velocities for step-up ($BR > 1$) and step-down ($BR < 1$) canyons and $\theta = 45°$. (**Top**) u_x; (**bottom**) u_y. Predictions with (solid red line) and without (dotted black line) the intermediate vortex sheet located on top of the lower building are compared to IDDES (dashed blue line).

The mean profiles represent an average over a primary canyon between the buildings ($-0.5 < x/W < 0.5$) and a secondary one above the lower building ($-1 < x/W < -0.5$ for the step-up canyon and $0.5 < x/W < 1$ for the step-down canyon). However, the

geometric constants for the entire canyon can be used to estimate the wind profiles within the subregions, $-1 < x/W < 0.5$, $-0.5 < x/W < 0.5$, $-1 < x/W < 0.5$, or $0.5 < x/W < 1$. The errors increase for the vertical profiles within the subregions but the basic trends are reproduced (see Figure A7).

3.4. Real Urban Areas

To test the applicability of the vortex method to real urban areas, two domains are considered: (i) a *homogeneous neighbourhood* (Whampoa, Hong Kong; Figure 1d) in which the building heights are relatively uniform; (ii) a *heterogeneous neighbourhood* (Central, Hong Kong; Figure 1e) in which building heights vary greatly.

3.4.1. Homogeneous Neighbourhood

The Whampoa neighbourhood includes two clusters of buildings (Figure 1d). The clusters are composed of ~ 20 non-rectangular (cruciform) buildings and separated by a central street canyon. They are used to define the vortex sheets.

Horizontal and vertical cross-sections of the vorticity magnitude are shown in Figure 11 for an external wind approximately parallel to the central street canyon ($\theta = 45°$). In the $x - y$ plane, strong vorticity is found around the periphery of each cluster and the central street canyon (panel a). In the $x - z$ plane, strong vorticity continues to be found at the ground and roof level (panel b). Spatial localisation of the vorticity is maintained for this neighbourhood. Analogously to the (effectively parallel) street canyons of Sections 3.1– 3.3, Figure 11 suggests that the continuous vorticity distribution be approximated with discrete vortex sheets at the ground, roof level and the periphery of each cluster. For simplicity, variations of the vorticity on the scale of individual buildings are neglected: it is assumed that the clusters are enclosed by uniform flat walls.

Baseline and extended sets of vortex sheets may be defined (Figure 1d) as

$$\Omega^{hom,base} \equiv \{(\Re^b, \omega_y), (\Re^t, \omega_y)\}, \tag{8a}$$

$$\Omega^{hom,extended} \equiv \Omega^{hom,base} \cup \Omega^{hom,sidewall}, \quad \Omega^{hom,sidewall} \equiv \cup_{i=1}^{5} (\Re^{s_i}, \chi_i \omega_z), \tag{8b}$$

where $\Re^{s_i}$ refers to the five sidewall vortex sheets and the indicator function $\chi_i = 1$ if sheet i is included in a specific arrangement (and zero otherwise). The baseline arrangement includes the top and bottom vortex sheets only; the extended arrangement also includes sidewall vortex sheets at the lower edge ($\Re^{s_1}$, $\Re^{s_2}$), leading-edge ($\Re^{s_3}$) and trailing edge ($\Re^{s_4}$) of each cluster as well as along the central street canyon ($\Re^{s_5}$). The piecewise constant vorticity distribution represented by Equation (8b) is not different in kind from $\Omega^{shallow}$ and Ω^{deep} or classical vortex dynamics models [19].

Given that the heights are approximately uniform and that $AR \sim 1$ for the central street canyon, $\Omega^{hom,base}$ may suffice. On the other hand, it is clear from Figure 11 that the vorticity structure is more complicated than that of a uniform street canyon. We examine the sensitivity to the inclusion of additional vortex sheets for $\Omega^{hom,extended}$ with N_s, the number of sidewall vortex sheets with $\chi_i = 1$. The absolute and relative errors are plotted against N_s, for $\theta = 45°$, the wind direction used to calculate the geometric constants, in Figure 12. The minimum, maximum and mean errors are calculated by considering all possible combinations of the $\Re^{s_i}$ for each value of N_s. The errors are largest when there are no sidewall vortex sheets, i.e., for $\Omega^{hom,base}$ or $N_s = 0$. For u_x, the best ($\varepsilon_r = 0.13$, $\varepsilon_a = 0.014$) and worst ($\varepsilon_r = 0.16$, $\varepsilon_a = 0.017$) sets are

$$\Omega^{best\,x} \equiv (\Re^{s_2}, \omega_z) \cup (\Re^{s_3}, \omega_z) \cup (\Re^{s_4}, \omega_z) \cup (\Re^{s_4}, \omega_z), \tag{9a}$$

$$\Omega^{worst\,x} \equiv (\Re^{s_1}, \omega_z). \tag{9b}$$

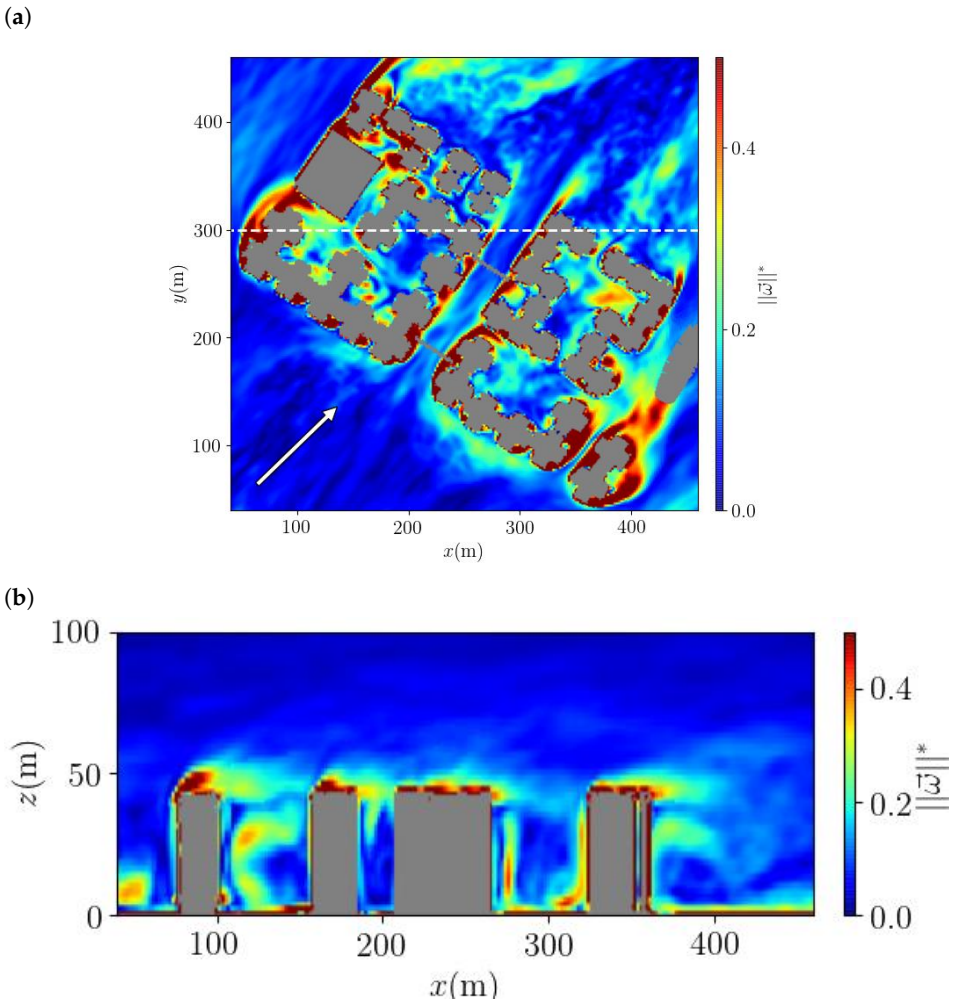

Figure 11. Time-averaged normalised vorticity magnitude for the homogeneous neighbourhood and an external wind at 45° (indicated by the arrow): (**a**) $x-y$ plane at $z/H = 0.5$; (**b**) $x-z$ plane at $y = 300$ m (indicated by the white dashed line in panel **a**).

Adding sidewall vortex sheets can degrade the accuracy of the u_x profiles, though the sensitivity is fairly weak. For u_y, the best and worst results are obtained from

$$\Omega^{best\,y} \equiv (\Re^{s_1}, \omega_z) \cup (\Re^{s_2}, \omega_z) \cup (\Re^{s_3}, \omega_z) \cup (\Re^{s_4}, \omega_z) \cup (\Re^{s_5}, \omega_z), \tag{10a}$$

$$\Omega^{worst\,y} \equiv (\Re^{s_3}, \omega_z). \tag{10b}$$

Adding a vortex sheet always decreases the errors for u_y. For both u_x and u_y, ε_a and ε_r improve by 35–55% when a single vortex sheet is added, i.e., from $N_s = 0$ to $N_s = 1$, but improvements for $N_s \geq 1$ are much smaller. Evidently, the top and bottom vortex sheets are more important than the sidewall and intermediate ones. This agrees with the analysis for the deep street canyon (see Appendix B).

Mean profiles (averaged over the computational domain but excluding the lateral buffer) for $\Omega^{best\,x}$ and $\Omega^{best\,y}$ are compared to the IDDES truth in Figure 13. The u_x profiles show limited sensitivity to the specification of the sidewall vortex sheets but the spread is greater for the u_y profiles. Except for the special cases of u_x at 90° and u_y at 0°, for which the mean velocity components are weak and the geometric constants for 45° inadequate (see Section 3.2), agreement with IDDES is relatively good for the best configuration (Equations (9a) and (10a)). Errors are generally smaller than those for the deep canyon. The relative and absolute errors are listed in Table A7.

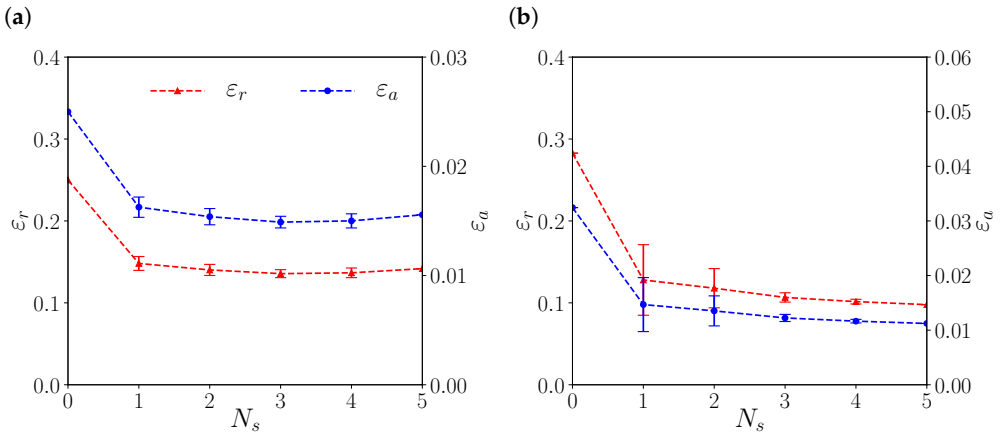

Figure 12. Mean absolute (ε_a) and relative (ε_r) errors against the number of sidewall vortex sheets, N_s, for $\theta = 45°$: (**a**) u_x; (**b**) u_y. The error bars represent the minimum and maximum errors for each ensemble of N_s sidewall vortex sheets. absolute errors are represented by blue lines; relative ones are denoted by red lines.

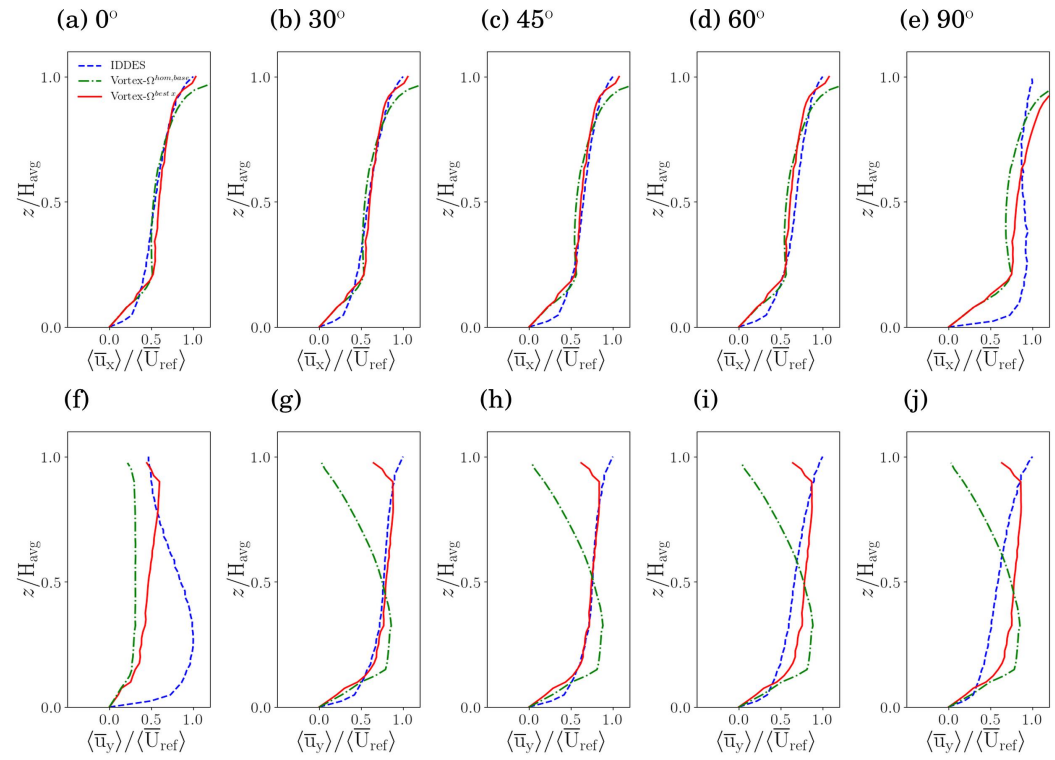

Figure 13. Vertical profiles of mean normalised velocities within the homogeneous domain. (**Top**) u_x estimated by $\Omega^{best\,x}$ (solid red line) and $\Omega^{hom,base}$ (dash-dotted green line); (**bottom**) u_y estimated by $\Omega^{best\,y}$ (solid red line) and a single vortex sheet ($\Omega^{worst\,y}$; dash-dotted green line). The IDDES profiles are plotted with a dashed blue line. The reference value, $\langle \bar{U}_{ref} \rangle$, was obtained by averaging the IDDES streamwise velocity at $z/H_{avg} = 1$. Geometric constants were calculated at 45°.

3.4.2. Heterogeneous Neighbourhood

The Central neighbourhood (Figure 1e) is comprised of two parts, the left half with two tall towers and the right half with shorter buildings of variable height. The domain may, therefore, be viewed as a sort of asymmetric canyon (i.e., a step-down canyon under a westerly wind and a step-up canyon under an easterly one). Only westerly and easterly winds are considered as they are the dominant wind directions: according to the wind rose for the Hong Kong Observatory's King's Park meteorological sta-

tion (https://www.weather.gov.hk/en/cis/region_climat/windrose.htm?&std=HKO, accessed on 19 November 2022), westerly and easterly winds occur 83% of the time. The agreement is unlikely to be significantly different for other wind directions. The results for the homogeneous neighbourhood (Figure 13) suggest that, except for winds at 0° and 45°, agreement is maintained over a wide range of wind directions; the buildings of the heterogeneous neighbourhood, however, are not perfectly aligned.

Cross-sections of the vorticity magnitude are plotted in Figure 14. In the horizontal section (panel a), strong vorticity appears around the tall buildings at the left and to a lesser extent within the street canyons at the right, but spatial localisation is weaker compared to the homogeneous domain (Figure 11). In the vertical section (panel b), the weaker localisation of the vorticity is more evident as values may be found away from the walls or ground. There is no evidence of multiple vortices inside deep canyons; indeed, coherent vortices are not easily discerned from streamlines in the vertical plane (not shown).

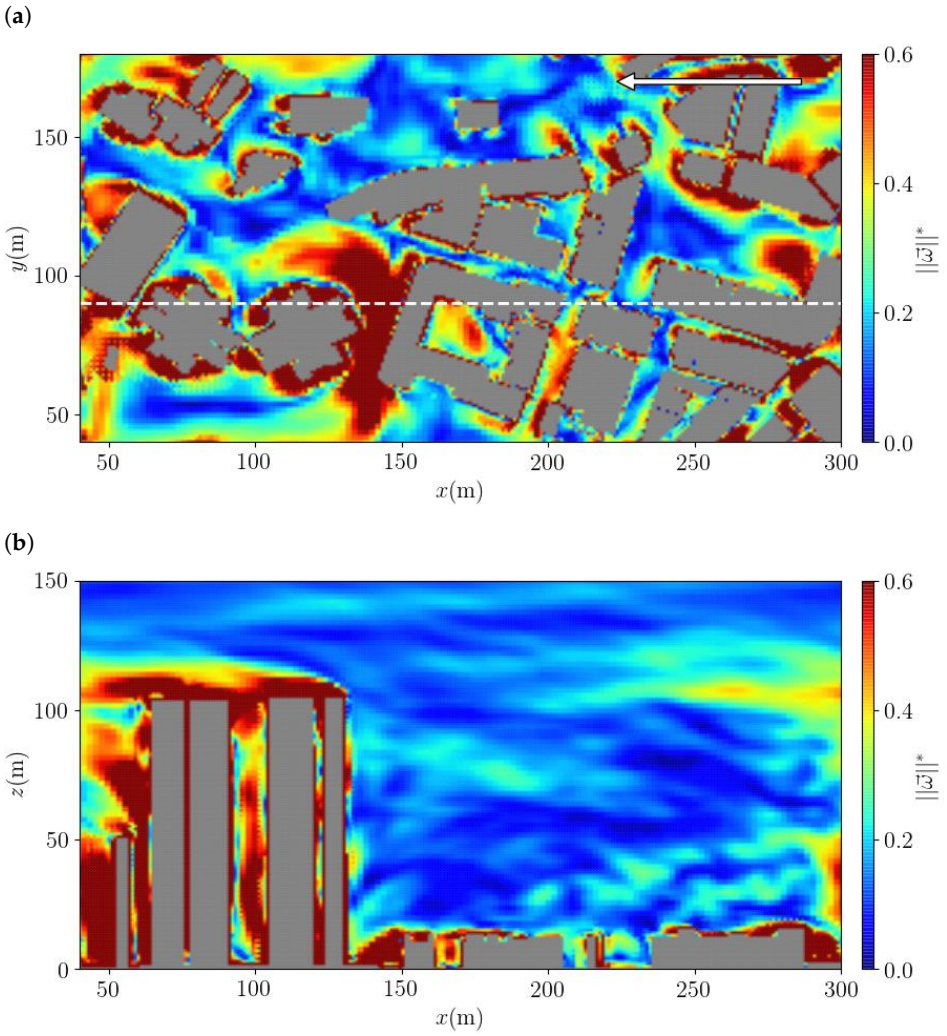

Figure 14. Time-averaged normalised vorticity magnitude for the Central neighbourhood and an external easterly wind (indicated by the arrow): (**a**) $x - y$ plane at $z = 10$ m; (**b**) $x - z$ plane at $y = 90$ m (indicated by the white dashed line in panel a).

Since spatial localisation persists for the heterogeneous domain, albeit in attenuated form, the vorticity field may be approximated with the discrete vortex sheets of Figure 1e. The approach follows that for the asymmetric canyon and homogeneous neighbourhood. First, the top and bottom vortex sheets, $\Re^b$ and $\Re^t$, are located on the ground and the rooftop of the tallest building. Second, sidewall vortex sheets, $\Re^{s_i}$, are introduced along

each of the nominal street canyons, the first ($\Re^{s1}$) between the left and right halves and the remainder ($\Re^{s2}$-$\Re^{s5}$) within the right half. They extend to the spanwise boundaries and top of the associated cluster. Third, intermediate vortex sheets, $\Re^{i_j}$, are located at the rooftops of the tallest building within each cluster in the right half, namely the front cluster ($\Re^{i_1}$, $H \sim 55$ m) and the back cluster ($\Re^{i_2}$, $H \sim 25$ m). They extend from the edge of the cluster to the boundaries. Hence the vortex set Ω^{inhom} Figure 1e) is defined as

$$\Omega^{inhom} \equiv \{(\Re^b, \omega_y), (\Re^t, \omega_y)\} + \Omega^{inhom,inter} + \Omega^{inhom,sidewall}, \tag{11}$$

$$\Omega^{inhom,inter} \equiv \cup_{j=1}^{2}(\Re^{i_j}, \chi_i \omega_y), \tag{12}$$

$$\Omega^{inhom,sidewall} \equiv \cup_{i=1}^{5}(\Re^{s_i}, \chi_i \omega_z). \tag{13}$$

The errors for u_x and u_y are minimised for the entire set of vortex sheets, i.e., $N_i = 2$ and $N_s = 5$. (For the precise dependence on N_i and N_s, see Appendix E, Figure A8).

Profiles for easterly and westerly winds are shown in Figure 15. For this inhomogeneous domain, different horizontal averages are taken: the entire domain excluding the buffer region, D_{whole}; the subregion covered by $\Re^{i_1}$, $D_{\Re^{i_1}}$ (i.e., the upper part of the right half); the subregion covered by $\Re^{i_2}$, $D_{\Re^{i_2}}$ (i.e., the lower part of the right half). In all cases, the profiles show a more complicated dependence on height than do the ones for the homogeneous domain (Figure 13). Nevertheless, good agreement with the IDDES reference is obtained for westerly and easterly winds, especially for D_{whole}, though the agreement is slightly better in the former case, which was also used to calculate the geometric constants. (The errors are summarised in Appendix F, Table A8). Despite the complexity of the heterogeneous domain and the weaker spatial localisation, the agreement is comparable to that for the homogeneous domain.

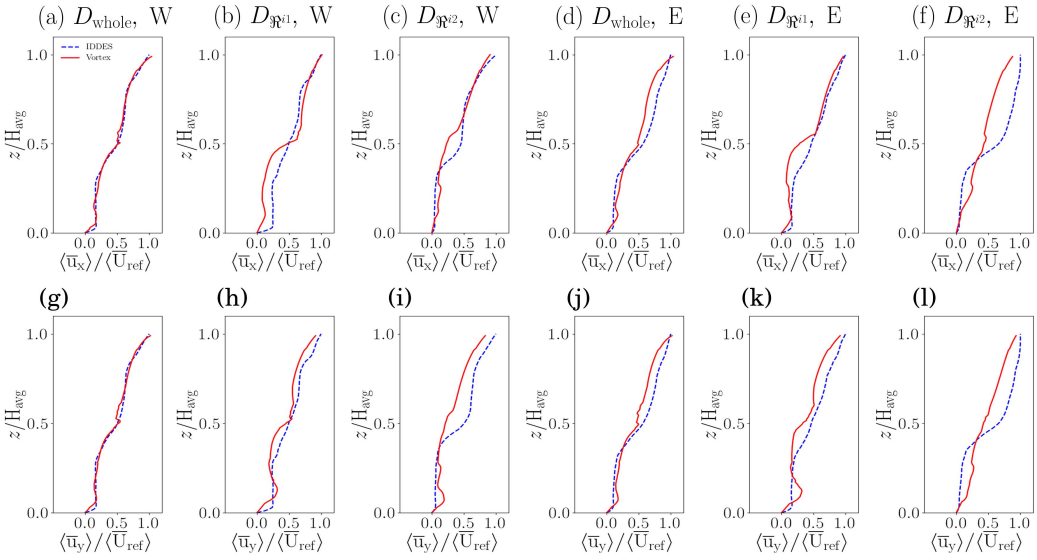

Figure 15. Vertical profiles of normalised mean velocities for the heterogeneous neighbourhood: (**top**) u_x; (**bottom**) u_y. The vertical profiles represent horizontal averages over: (**a**,**d**,**g**,**j**) the entire domain (excluding lateral buffer); (**b**,**e**,**h**,**k**) $\Re^{i1}$ (shown in red in Figure 1e); (**c**,**f**,**i**,**l**) $\Re^{i2}$ (shown in violet in Figure 1e). Westerly results are shown at the left (**a**–**c**,**g**–**i**), easterly results at the right (**d**–**f**,**j**–**l**). The reference value, $\langle \bar{U}_{\mathrm{ref}} \rangle$, was obtained by averaging the IDDES streamwise velocity at $z/H_{\mathrm{avg}} = 1$. The geometric constants correspond to the westerly case and the average over the entire domain, D_{whole}. Agreement is degraded for the averages over the subdomains, $D_{\Re^{i1}}$ and $D_{\Re^{i2}}$.

4. Stratification

The assumption of neutral flow, which is commonly made in urban CFD and wind engineering, is not always satisfied. On the one hand, solar heating and energy exchange with buildings may lead to convectively unstable conditions [65]. On the other hand, changing meteorological conditions may yield stable stratification [66]. Since the temperature does not project directly onto the vorticity, the vortex sheets cannot provide a complete description of the flow, even in the idealised limit of negligible nonlinearity and perfect spatial localisation. The influence of stratification on the applicability of the vortex method is, therefore, examined for a unit-aspect-ratio street canyon with bottom heating (or cooling).

Following [58], the stratification is characterised with the bulk Richardson number,

$$\mathrm{Rb} = \left(\frac{g}{\overline{T}}\frac{T_{roof} - T_{bottom}}{H}\right) \Big/ \left(\frac{U_{\mathrm{ref}}}{H}\right)^2, \tag{14}$$

where T_{roof}, T_{bottom}, $\overline{T}$ are the roof level, ground and mean canyon temperatures. Results for several values of $\Delta T \equiv T_{bottom} - T_{inlet}$ (Table 3) are reported below.

Table 3. Stratification parameters. The temperature at the inflow boundary, T_{inlet}, is fixed at 300 K.

Stratification	Stable (K)	Neutral (K)	Unstable (K)
ΔT	$-8, -6, -4, -2$	0	2, 4, 6, 8
Rb	0.38, 0.29, 0.19, 0.09	0	$-0.09, -0.19, -0.30, -0.39$

Flow structures for stable ($\Delta T < 0$) and unstable ($\Delta T > 0$) stratification are illustrated in Figure 16. As in previous studies [51–53], the flow within the canyon is dominated by a central vortex. Differences among the ΔT are most noticeable near the roof level: while the streamlines remain confined within the canyon for stable stratification (panel a), they extend slightly into the shear layer for unstable stratification (panel d). The spatial localisation of the vorticity magnitude is not significantly affected by the stratification. Strong vorticity at the top, bottom and sidewalls is maintained for stable stratification (panel b), but the roof-level vorticity is weaker for unstable stratification (panel e). The TKE in the interior is relatively weak in both cases (panels c,f), suggesting that the nonlinear contribution to the flow is not substantially different from the neutral case (Figure 4i).

From the flow structure, the vorticity sheets may be defined similarly to the shallow and deep canyons, i.e., the set $\Omega^{shallow}$ is adopted (Figure 1a). At $\theta = 45°$, the projection onto the vortex sheets is similar for stable and neutral cases (the weights differ by less than 10%); for unstable stratification, the projection onto the top vortex sheet is weaker and the variation among the weights is smaller.

The estimated profiles follow the actual ones reasonably well for all values of Rb (Figure 17). Relative errors are shown in Figure 18. They are approximately constant for $\mathrm{Rb} < 0$ and $\mathrm{Rb} > 0$. Accuracy decreases for unstable stratification, but is largely unaffected by stable stratification.

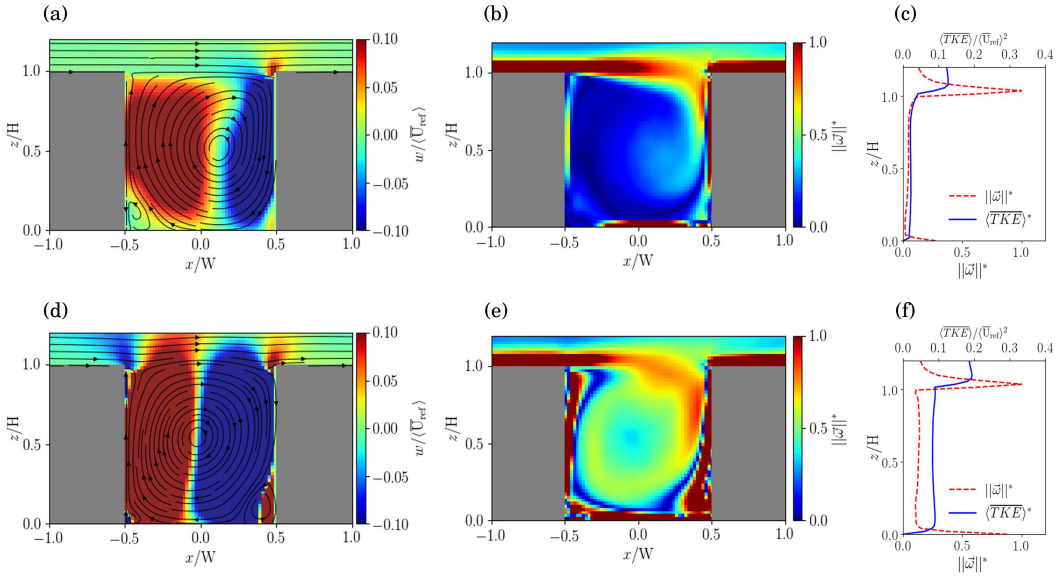

Figure 16. Flow structures for stratified flow within an $AR = 1$ street canyon: (**top**) stable conditions (Rb $= 0.38$); (**bottom**) unstable conditions (Rb $= -0.39$). (**a**,**d**) Spatially averaged streamlines; (**b**,**e**) spatially averaged vorticity magnitude; (**c**,**f**) vertical profiles of normalised TKE and vorticity magnitude. See Figure 4 for additional figure details.

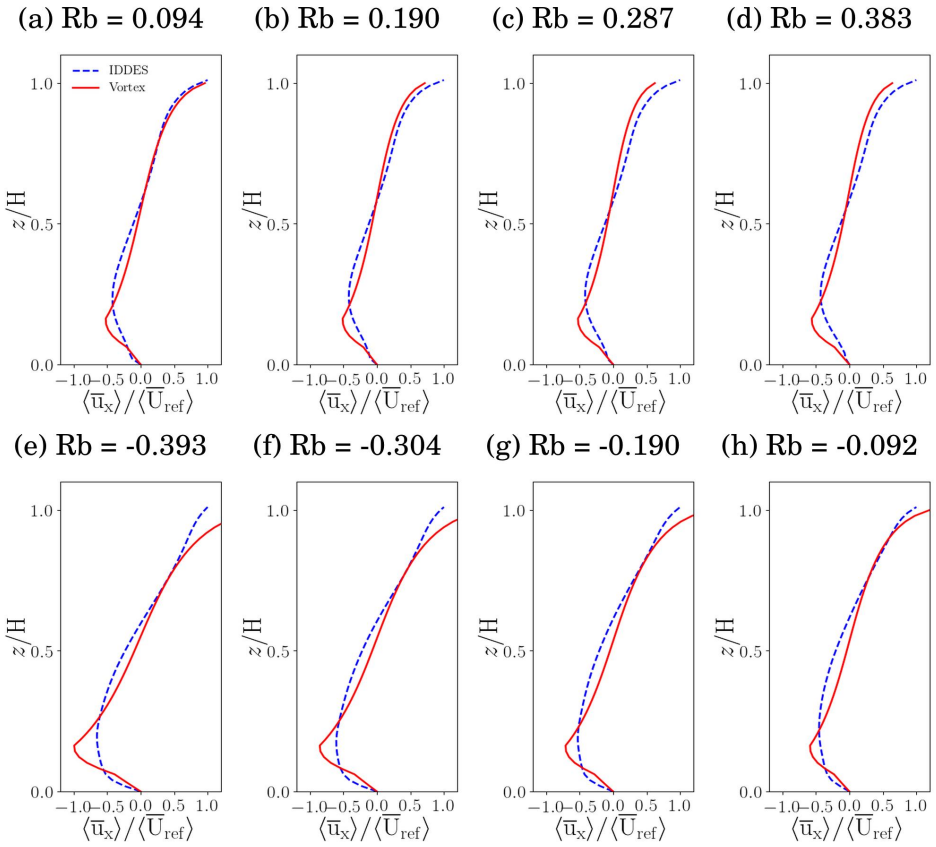

Figure 17. Vertical profiles of normalised streamwise velocities for $AR = 1$ and different Rb. (**Top**) Stable stratification; (**bottom**) unstable stratification. Predicted (solid lines) and IDDES (dashed lines) results are compared at $\theta = 45°$; the geometric constants were calculated at 0°.

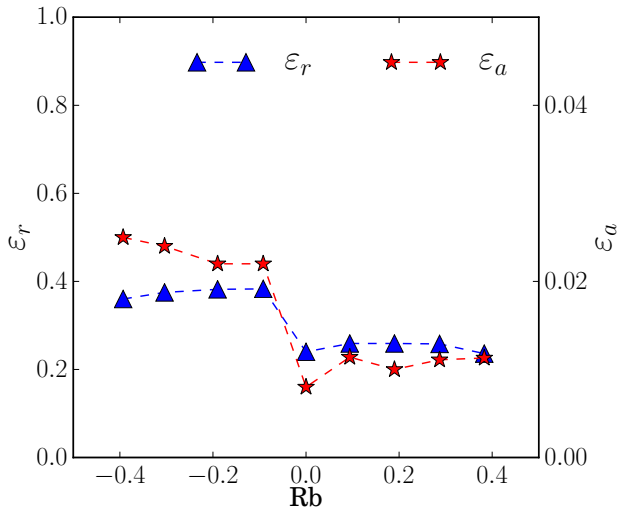

Figure 18. Canyon-averaged relative error in u_x versus Rb.

5. Discussion

The accuracy of the vortex method depends on the extent to which the vorticity field is localised within vortex sheets and fluctuations are strongly influenced by linear dynamics. For a single street canyon, the vorticity components are strongly localised at the walls [18,21] and the linear term describing the straining of fluctuations by the mean flow can be used to estimate the growth rate of perturbations [32], while the linear production term in the TKE budget is comparable to the nonlinear one near the roof level [33]. The appropriateness of these assumptions is less obvious for the more realistic flows considered in this study: multiple vortices appear inside deep canyons; vortex sheets may be more difficult to define for asymmetric canyons or real urban neighbourhoods in which the building height or shape is not uniform; stratified flows may not be adequately described by the vorticity.

Nevertheless, errors do not increase significantly. Whereas the canyon-averaged relative error in the streamwise velocity is ∼10–20% for a single street canyon, it is ∼ 20% for the shallow canyons, ∼ 40% for the deep canyons, and ∼ 30% for the homogeneous neighbourhood and ∼3–15% for the heterogeneous one. The robustness of the vortex method for the different geometries can be explained as follows. First, the building geometries are sufficiently regular that strong vorticity gradients at the walls are maintained. This can be seen in cross-sections of the vorticity magnitude (e.g., Figures 4, 6, 9, 11 and 14). Since the buildings are exactly (for the idealised domains) or approximately (for the realistic ones) cuboidal, it is reasonable that vorticity gradients should be maintained away from the roof level. This may no longer be the case when there is strong height variability; however, the buildings of the heterogeneous domain can be subdivided into distinct clusters with approximately uniform building height. Errors increase for the deep canyon because the existence of multiple vortices is not taken into account. The accuracy is not completely compromised, possibly because the secondary vortex is weak. When an intermediate vortex sheet is added to the mid-plane of the canyon, the inflection point in the vertical profiles is captured and the canyon-averaged streamwise relative error decreases from ∼ 60% to ∼ 30% for $AR = 3$.

Second, it is plausible that the linear contribution to fluctuations should continue to be more important for more realistic geometries. Ref. [67] showed that, for a staggered array of cubes, the magnitude of the linear production term is larger than that of the nonlinear term near the roof level and roughly comparable inside the canopy, as with a single street canyon. Physically, one may expect the linear term to make a significant contribution where there is a strong mean circulation, as with a single street canyon or a regular building array.

The validity of these assumptions is less assured for stratified flow. Although spatial localisation at the ground and roof level persists for the single street canyon under stable and unstable stratification, the nature of turbulence within the canopy changes in the unstable case as convective plumes is generated [68]. One may, therefore, surmise that the linear contribution is less important for bottom heating; nevertheless, there is still some residual skill as the streamwise relative error is $\sim 40\%$ for the unstable cases. This may be attributed to the fact that, despite the emergence of convective plumes, the mean flow inside the canopy still reflects the building geometry (as seen, for example, in the horizontal streamlines). Accuracy for stable stratification is nearly unchanged, as may be expected from the weak dependence of the mean flow and turbulence statistics on the bulk Richardson number for bottom cooling.

The preceding arguments suggest that the vortex method should extend to domains with regular, canyon-like features and stable stratification. For these domains, vortex sheets may be located at the top, bottom and periphery of each building cluster. In the general case, the definition of the clusters may not be unambiguous; however, an objective, multiscale procedure could be developed. Comparisons with training data could be made to select the vortex sheets. In the absence of training data, the magnitude of the basis functions could be compared, as with the objective procedure for selecting a reduced set of vorticity sheets (Appendix B). That procedure, which was developed and tested for a deep canyon only, could be refined further. Although sensitivity to the number of vorticity sheets was examined for the realistic domains, the current study is primarily concerned with the applicability of a reduced basis to the estimation of mean winds rather than the optimal projection.

6. Conclusions

This work shows that mean wind profiles within realistic urban canopies can be estimated without solving the governing equations via computational fluid dynamics. Instead, basis functions obtained from approximating the vorticity field with discrete vortex sheets and solving the associated three-dimensional Poisson equation can be used to estimate mean wind profiles after calibration with training data for a specific wind direction. Mean streamwise (u_x) and spanwise (u_y) velocity profiles show good agreement (i.e., canyon-averaged relative errors of $\sim$10–40%) with IDDES for shallow ($AR < 1$), deep ($AR = 3$), asymmetric (step-up and step-down) and realistic canyons. For a single street canyon, errors for neutral and stable cases are comparable, but larger by around a factor of two for unstable stratification.

The primary implication of this work is that the computational cost of estimating mean velocity profiles for urban flows can be greatly decreased through a dimensional reduction procedure based on discrete vortex sheets. Whereas building-resolving CFD requires considerable computational resources, the vortex-method calculations described in this paper required less than 6 s of CPU time (Intel i5-6500, single core only). Nevertheless, the vortex method is not a replacement for CFD or any first-principles prediction method. Although it is derived from the equations for inviscid dynamics, the vortex method is essentially a statistical method: it requires training data and is applied to the horizontal (spatial) average. As such, it is similar in spirit to machine learning methods which seek to develop a reduced basis (e.g., the neurons of a neural network); however, the present approach is not purely statistical. Its starting point is one of the defining features of urban flows, namely the strong influence of the building geometry on the mean circulation. This physical idea is embodied in the key assumptions underlying the method, namely spatial localisation of the vorticity at the walls and a strong (i.e., leading order) contribution of the linear contribution to turbulent fluctuations (see Section 5 for further discussion). The good performance of the vortex method suggests that these are reasonable assumptions for realistic urban canopies.

The present study is primarily concerned with whether the vortex method, which was developed for a unit-aspect-ratio street canyon, extends to more realistic configurations.

Future work should consider additional geometries and meteorological conditions. The homogeneous and heterogeneous neighbourhoods of Section 3.4 are more realistic than the street canyon geometries; however, they may not be representative of sparsely urbanised areas. The sensitivity to stratification, or more precisely, bottom heating or cooling, may likewise differ from that for a unit-aspect-ratio street canyon. Application to more irregular domains would benefit from an objective method for determining the vortex sheets. Since the geometries considered herein are street-canyon-like, the vortex sheets may be located at the walls and the rooftop or, in the case of a nominal building cluster, along the periphery and at the rooftop of the tallest building. Another interesting extension would be the estimation of mean wind profiles above the canopy. The vortex method should also apply above the roof level if the key assumptions are satisfied. Clearly, this is unlikely to be true far away from the rooftops (i.e., in the inertial layer), where the direct influence of the roughness can no longer be felt. Preliminary results (not shown) indicate that the vortex method can be used to estimate mean profiles for regular street canyons or building arrays up to $z/H \sim 2$.

The low computational cost of the vortex method means that it is potentially well-suited to practical applications in which computational speed is crucial. First, it may be used for fast dispersion modelling. To the extent that pollutant dispersion from deep canopies is controlled by the mean velocity, for example, [69], a model based on the mean wind profiles induced by the actual building geometry could be preferable to idealised models that assume spatially uniform winds or an exponential or log profile. A fast dispersion model with spatially varying three-dimensional winds (For a regular building array, estimates of the mean vertical velocity component show comparable accuracy to those for the horizontal ones (not shown).) (obtained through different local averages) is currently being developed. Second, the vortex method could be used to extrapolate in situ measurements, which are rarely available inside the canopy. In theory, such data could be extrapolated using CFD, but even with advances in computing power, this is a cumbersome procedure that could not be easily performed in the field. The vortex method, by contrast, presents minimal computational challenges and requires less initialisation data (i.e., a complete set of boundary conditions and initial conditions instead of the vortex sheet strengths or a reference velocity scale). Finally, the vortex method could be used to generate data for more accurate models. Inflow wind profiles would be one application.

Author Contributions: H.W.: Writing-Original draft preparation, Software, Validation, Visualization. E.F.-C.: Software, Validation, Reviewing. K.N.: Conceptualization, Supervision, Methodology, Formal analysis, Writing—Reviewing & Editing, Project administration, Funding acquisition. All authors have read and agreed to the published version of the manuscript.

Funding: This research was supported by the Research Grants Council of Hong Kong (CityU 11304517), City University of Hong Kong (Project 7005585) and the Environmental Protection Department of Hong Kong (Reference 20-02153).

Institutional Review Board Statement: Not applicable.

Informed Consent Statement: Not applicable.

Data Availability Statement: Not applicable.

Conflicts of Interest: The authors declare that they have no known competing financial interests or personal relationships that could have appeared to influence the work reported in this paper.

Appendix A. Vortex Dynamics and Vortex Method

The vorticity is defined as

$$\vec{\omega} = \vec{\nabla} \times \vec{u}, \tag{A1}$$

where $\vec{\omega} = (\omega_x, \omega_y, \omega_z) = \left((\frac{\partial u_z}{\partial y} - \frac{\partial u_y}{\partial z}), (\frac{\partial u_x}{\partial z} - \frac{\partial u_z}{\partial x}), (\frac{\partial u_y}{\partial x} - \frac{\partial u_x}{\partial y}) \right)$ is the vorticity. In three dimensions, the velocity may be expressed in terms of the vector potential, $\vec{A}$,

$$\vec{u} = \vec{\nabla} \times \vec{A}, \tag{A2}$$

whence

$$\vec{\omega} = \nabla^2 \vec{A}, \tag{A3}$$

after specifying $\vec{\nabla} \cdot \vec{A} = 0$. Assuming suitable boundary conditions for $\vec{A}$, i.e., free slip or constant $\vec{A}$ along surfaces, the Poisson equation for a delta function source,

$$\nabla^2 G(\vec{x}|\vec{x}') = \delta(\vec{x} - \vec{x}'), \tag{A4}$$

may be solved to yield the Green's function or potential flow solution, $G(\vec{x}|\vec{x}')$. The solution for a general vorticity source, $\vec{\omega}$, is obtained from linear superposition,

$$\vec{A}(\vec{x}) = \iiint_D G(\vec{x}|\vec{x}')\vec{\omega}(\vec{x}')d\vec{x}'. \tag{A5}$$

In vortex dynamics, $\vec{\omega}$ is approximated, leading to evolution equations for the vortex motion. In the present case, the vorticity distribution is approximated with a finite number of uniform vortex sheets which are fixed in space. We focus on Green's functions for a set of vortex sheets with constant vorticity. Each Green's function may be viewed as the response to a vortex sheet with vorticity component ω_k and unit magnitude; for the jth vortex sheet, it implies a velocity basis function, v_i^{j,ω_k}. Since we focus on the time-averaged velocity profiles, the vortex sheets are assumed to be independent and nonlinear effects are neglected. Hence the mean velocity profiles may be obtained by summing over the spatially averaged basis functions, $\langle v_i^{j,\omega_k} \rangle$.

In the prediction Equation (1), the basis functions are weighted by a factor, α^{j,ω_k}, which may be obtained through a calibration procedure. The response to an arbitrary vortex sheet depends on the vortex sheet strength or circulation. The circulation can be related to the tangential velocity at the vortex sheet, $\langle u_i \rangle_s$ by

$$\gamma^{j,\omega_k} = \langle u_i \rangle_s, \tag{A6}$$

after ignoring dimensional scaling factors. (More formally, the circulation is calculated by enclosing the vortex sheet with a loop of infinitesimal thickness.) From $\langle u_i \rangle_s$, which is analogous to a boundary condition in vortex dynamics, the weights may be defined by

$$\alpha^{j,\omega_k} \equiv C^{j,\omega_k} \langle u_i \rangle_s. \tag{A7}$$

The geometric constants C^{j,ω_k}, which incorporate dimensional scaling factors omitted from Equation (A6), are taken to be independent of the flow. They are calculated by minimising the residual between the predicted mean velocity profile, Equation (1) and a true profile (see Equation (3)).

The vortex solution in the interior, $\langle u_i \rangle(z)$, is matched to the log profile

$$u_i(z) = \frac{u_{i*}}{k} \log \frac{z + z_0}{z_0}, \tag{A8}$$

where k is the von Kármán constant and z_0 is the roughness length. The no-slip boundary condition, $u_i(z = 0) = 0$, is automatically satisfied. The friction velocity is given by

$$u_{i*} = \kappa \frac{U_{i,ref}}{\log\left(\frac{z_{\text{ref}} + z_0}{z_0}\right)}. \tag{A9}$$

where $U_{i,ref} \equiv \langle u_i(z_{\text{ref}})\rangle$ is the mean velocity at reference height, z_{ref}. Within the interval $0 \le z \le z_b$, the mean profile is calculated as

$$\langle u_i(z)\rangle = \frac{z}{z_b}\langle u_{i,vortex}\rangle + \frac{z_b - z}{z_b}\langle u_{i,log}\rangle, \tag{A10}$$

where $\langle u_{i,log}\rangle$ and $\langle u_{i,vortex}\rangle$ refer to Equations (A8) and (1).

Appendix B. Selecting a Reduced Set of Vorticity Sheets

Determining a reduced set of vorticity sheets is desirable, but physical intuition can only be invoked in special cases such as a single street canyon [18] or other idealised domains. Nevertheless, the potential contribution of a reduced set can be evaluated, without reference data, by comparing the basis functions. The procedure is illustrated below for $AR = 3$.

First, the contributions of the different vortex sheets for $AR = 3$ are compared in Table A1, which lists the canyon-averaged speeds induced by each vortex sheet, $\langle|u_i^j|\rangle$, where j indexes the sheets. Since we wish to characterise the strength of the response to each vortex sheet, the canyon-averaged absolute value (L1 norm) is taken; the same average has been used to diagnose flow-regime transitions within street canyons [21]. For each vortex sheet and vorticity component (i.e., vorticity sheet), vorticity of unit magnitude and $\langle|u_i^j|\rangle$ is normalised by the maximum over all j. For convenience, the entries used to define the reduced set, Ω^{deep}, are highlighted. The induced response from them is larger than that from the neglected contributions (and in most cases, significantly larger).

Table A1. Spatially averaged velocities for different vortex sheets, vorticity components and $AR = 3$. The normalisation constant is the maximum value for the entire set of vortex sheets.

Ground level	$\Re^b, \omega_x$	$\Re^b, \omega_y$	$\Re^b, \omega_z$
$\langle u_x\rangle / u_{x,max}$	0.0	5.1×10^{-1}	1.2×10^{-11}
$\langle u_y\rangle / u_{y,max}$	2.8×10^{-1}	0.0	6.6×10^{-9}
Roof level	$\Re^t, \omega_x$	$\Re^t, \omega_y$	$\Re^t, \omega_z$
$\langle u_x\rangle / u_{x,max}$	0.0	1.0	7.2×10^{-12}
$\langle u_y\rangle / u_{y,max}$	5.5×10^{-1}	0.0	5.5×10^{-10}
Side wall	$\Re^s, \omega_x$	$\Re^s, \omega_y$	$\Re^s, \omega_z$
$\langle u_x\rangle / u_{x,max}$	0.0	4.2×10^{-2}	1.1×10^{-11}
$\langle u_y\rangle / u_{y,max}$	2.3×10^{-2}	0.0	1.0

A complete set of vorticity sheets is used to define the set, $\Omega^{complete}$. Results for Ω^{deep} and $\Omega^{complete}$ are compared in Figure A1.

The profiles nearly coincide. The deviation between them is characterised using ε_r (after letting $\Omega^{complete}$ denote the nominal truth). In Table A2, $\varepsilon_r \sim 0.06\%$ for u_x and 1.8% for u_y. We conclude that the inclusion of additional vorticity sheets, which require more a priori information, has little effect on the accuracy.

Table A2. Relative errors between predicted mean profiles obtained using Ω^{deep} and $\Omega^{complete}$.

	0°	**30°**	**45°**	**60°**	**90°**
u_x	0.069	0.072	0.140	0.209	0.084
u_y	0.0085	0.0041	0.0019	0.0028	0.0034

A rough estimate of the relative importance of each vortex sheet can be obtained by considering the ratio of the sums, i.e.,

$$r = \frac{\sum_{j=1}^{N_s} \sum_{k=1}^{3} \delta_{j,k} \langle u_i^{j,\omega_k} \rangle}{\sum_{j=1}^{N_s} \sum_{k=1}^{3} \langle u_i^{j,\omega_k} \rangle} \tag{A11}$$

where u_i^{j,ω_k} is the velocity induced by the ω_k vorticity component of the jth vortex sheet, N_s is the number of vortex sheets, and $\delta_{j,k} = 1$ for a retained vortex sheet and 0 otherwise. For $\Omega^{complete}$, $\delta_{j,k} = 1$. For Ω^{deep}, $r = 32\%$ for u_x and 5.6% for u_y. The r values are roughly comparable to the actual relative errors listed in Table A2. Hence we conclude that a reduced set of vorticity sheets can be determined from analysis of the basis functions: additional CFD data is not required. Given the assumption of linearity that underlies the vortex method and the relative importance diagnostic, Equation (A11) may be used to assess the appropriateness of a reduced set of vorticity sheets for flows in which the vortex method should be applicable.

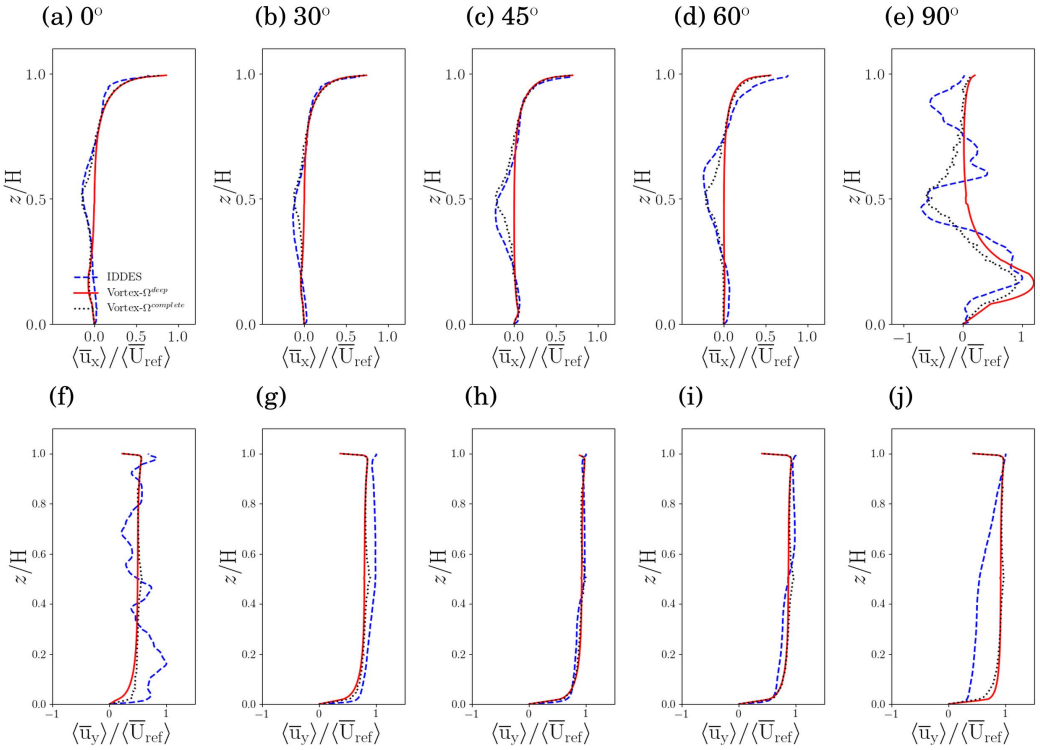

Figure A1. (**a**–**j**) Vertical profiles of normalised velocities within the deep canyon ($AR = 3$) for the complete set of vortex sheets $\Omega^{complete}$ (black dotted line), the reduced set Ω^{deep} (red line), and the IDDES baseline (blue line).

Appendix C. Sensitivity to Meshing and Wall Function

The sensitivity of the fine-scale vorticity structure to the numerical configuration is examined. The baseline configuration (R-base) follows the procedure employed for the shallow canyons (Section 3.1), e.g., grid resolution $\Delta = 1$ m away from the walls and $\Delta = 0.5$ m at the walls, Ref. [42] wall function (*nutUSpaldingWallFunction* in OpenFOAM), and free-stream velocity $U_\infty = 3\,\mathrm{m\,s^{-1}}$ at the upper lid. Other cases are summarised in Table A3.

Table A3. Summary of the sensitivity tests for the AR=1 canyon. For R-wall, OpenFOAM's *nutkWallFunction* is used.

Run	Resolution Δ	Mesh Size in the Vicinity of a Wall	Wall Function	U_∞
R-base	1.0 m × 1.0 m × 1.0 m	0.5 m × 0.5 m × 0.5 m	*nutUSpaldingWallFunction*	3 m s^{-1}
R-grid1	0.5 m × 0.5 m × 0.5 m	0.25 m × 0.25 m × 0.25 m	*nutUSpaldingWallFunction*	3 m s^{-1}
R-grid2	1.0 m × 1.0 m × 1.0 m	0.25 m × 0.25 m × 0.25 m	*nutUSpaldingWallFunction*	3 m s^{-1}
R-Re	1.0 m × 1.0 m × 1.0 m	0.5 m × 0.5 m × 0.5 m	*nutUSpaldingWallFunction*	10 m s^{-1}
R-wall	1.0 m × 1.0 m × 1.0 m	0.5 m × 0.5 m × 0.5 m	*nutkWallFunction*	3 m s^{-1}

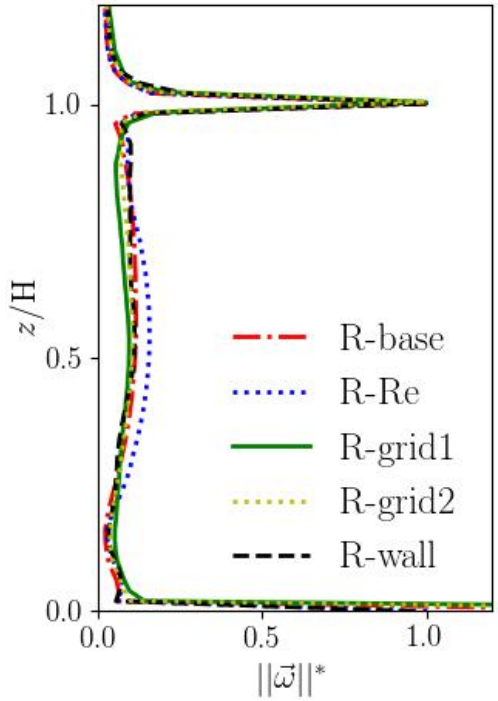

Figure A2. Vertical profiles of the normalised vorticity magnitude for the numerical configurations of Table A3 and an external wind at 0°.

Vertical profiles of the normalised vorticity magnitude are compared in Figure A2. The differences are largest in the interior and relatively small at the top and bottom. This is notable because the mean velocity profiles are calculated from vortex sheets defined at solid surfaces. The sensitivity of the vortex sheet strengths to the numerical configuration is examined in Table A4. For the top, bottom and middle vortex sheets, the normalised vortex sheet strengths are compared. The differences among configurations are ∼10–20%. The discrepancy with respect to the baseline increases for the *nutkWallFunction* and the sidewall and bottom vortex sheets. Nonetheless, the vortex sheet strengths show limited sensitivity to the numerical configuration.

The vortex sheet strengths listed in Table A4 are used in the prediction of the mean velocities. Figure A3 shows that the vertical profiles of u_x agree well for the different configurations. Indeed the configurations show comparable agreement with wind-tunnel data (Figure A4). This is confirmed by calculating absolute and relative errors (Table A5): the relative errors are ∼ 10–20%, in agreement with Table A4. We conclude that, on account of the linearity of the prediction Equation (1), the predicted mean velocity profiles do not show marked sensitivity to the numerical configuration.

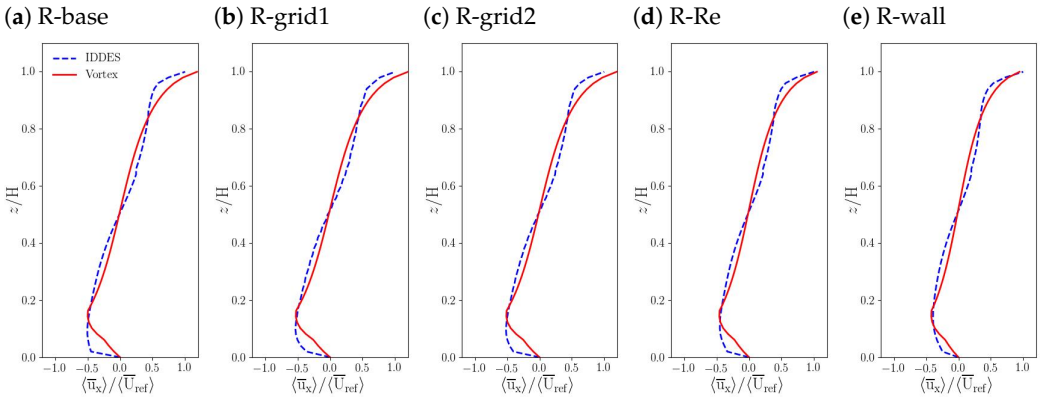

Figure A3. Vertical profiles of normalised streamwise velocities for $AR = 1$ and $\theta = 0°$. Predicted profiles (solid lines) were obtained from the vortex sheet strengths of Table A4; they all show similarly good agreement with the IDDES reference (dashed lines).

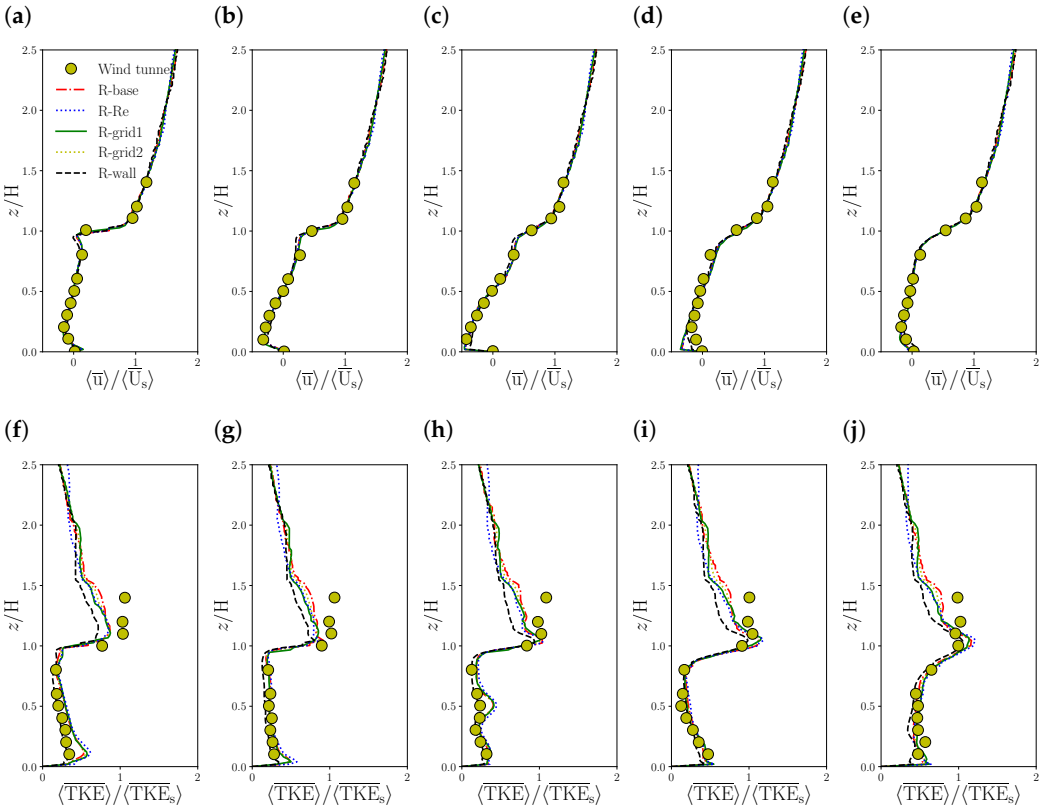

Figure A4. As in Figure 2, but for the runs of Table A3. Validation of the IDDES model (OpenFOAM) for neutral flow over a 2-D street canyon. Normalised mean streamwise velocity and TKE validation of IDDES (solid line) against wind tunnel experiment [54] (filled circles) at (**a**,**f**) $x/W = -0.4$; (**b**,**g**) $x/W = -0.25$; (**c**,**h**) $x/W = 0$; (**d**,**i**) $x/W = 0.25$; (**e**,**j**) $x/W = 0.4$. Reference values for the streamwise velocity and TKE, $\langle \overline{U_s} \rangle$ and $\langle \overline{TKE_s} \rangle$, represent averages of the IDDES data over the shear layer, $1 \leq z/H \leq 1.5$.

Table A4. Normalised vortex sheet strengths for the AR=1 canyons, $\langle u_i \rangle_s / U_{\text{ref}}$. The tangential velocity is averaged over each vortex sheet.

Vortex Sheet	Velocity Component	R-Base	R-Grid1	R-Grid2	R-Re	R-Wall
$(\Re^t, \omega_y)$	u_x	1.0	1.0	1.0	1.0	1.0
$(\Re^t, \omega_y)$	u_x	0.50	0.53	0.51	0.45	0.42
$(\Re^s, \omega_z)$	u_y	0.15	0.13	0.14	0.15	0.18

Table A5. Absolute and relative errors for the predicted profiles of Figure A3. $\varepsilon_a, \varepsilon_r$ are averaged over the entire canyon.

		R-Base	R-Grid1	R-Grid2	R-Re	R-Wall
u_x	ε_a	0.018	0.016	0.017	0.015	0.012
	ε_r	0.35	0.32	0.33	0.32	0.31

Appendix D. Grid Convergence

Grid convergence for the idealised canyons is examined using AR = 1 and the numerical configuration of Section 2.2. Two grids are examined: a coarse one with a base resolution away from the walls of $\Delta = 1$ m and a fine one with base resolution $\Delta = 0.5$ m. Vertical profiles of the mean streamwise velocity at 0° (Figure A5) nearly coincide for the two grids: the difference is $\sim 2\%$ over the entire canyon.

The grid convergence index (GCI; e.g., [70]) is defined as

$$GCI = F_s \frac{\epsilon_{rms}}{r^p - 1}, \tag{A12}$$

where $F \equiv 3$ and $p \equiv 2$ are empirical constants, ϵ_{rms} is the root-mean-square relative error between simulations with coarse and fine resolution, and r is the ratio of grid sizes. For a time-averaged velocity field, u_i, whose elements are indexed by i,

$$\epsilon_{rms} = \left(\frac{1}{N} \sum_{i=1}^{N} \epsilon_{i,c}^2 \right)^{\frac{1}{2}}, \tag{A13}$$

where

$$\epsilon_{i,u} = \frac{u_{i,coarse} - u_{i,fine}}{u_{i,fine}}. \tag{A14}$$

The GCI over the canyon is 1.2%, which is comparable to the value for the medium grid of the street-canyon study of [70]. Grid convergence for the realistic canyons is examined using the heterogeneous domain (Figure 1d). The GCI over the canyon is 1.0%. We, therefore, conclude that $\Delta = 1$ m is sufficient.

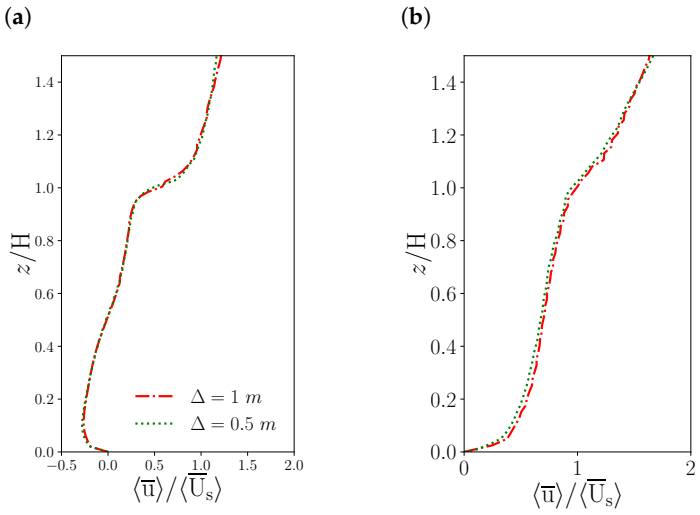

Figure A5. Vertical profiles of temporally and spatially averaged normalised velocity for two different resolutions. (**a**) a 2-D street canyon (*AR* = 1); (**b**) a realistic canyon (Figure 1d). Finer grid sizes ($\Delta = 0.5$ m) are represented by green dotted lines; coarser grid sizes ($\Delta = 1$ m) are indicated by red dash-dotted lines.

Appendix E. Supplementary Figures

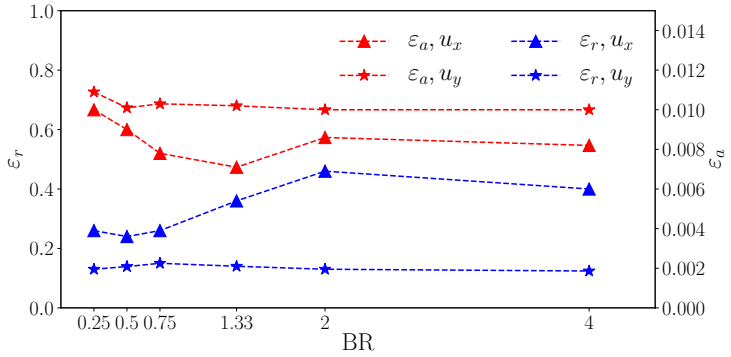

Figure A6. Absolute (ε_a) and relative (ε_r) errors versus BR for the asymmetric canyons. ε_a is normalised by U_{ref} (see Equation (4)).

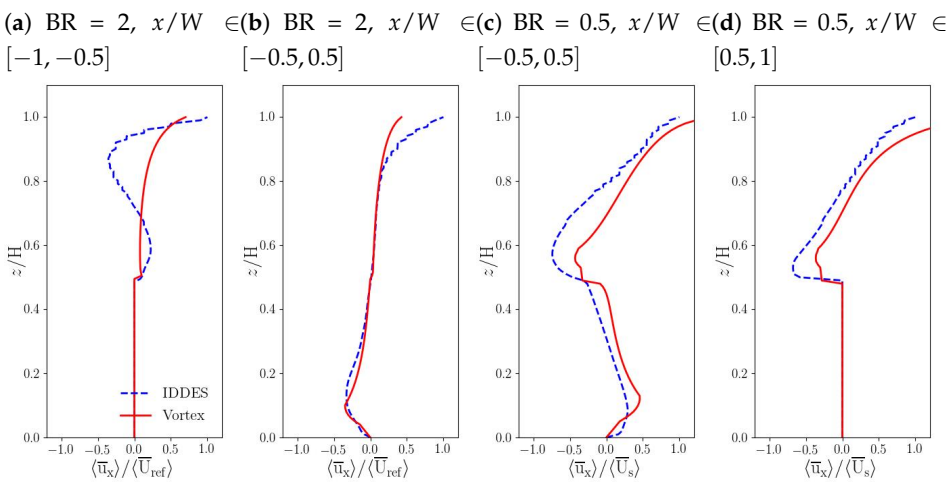

Figure A7. As in Figure 10, but for the streamwise velocity component over the subregions. (**a**,**b**) step-up canyon; (**c**,**d**) step-down canyon.

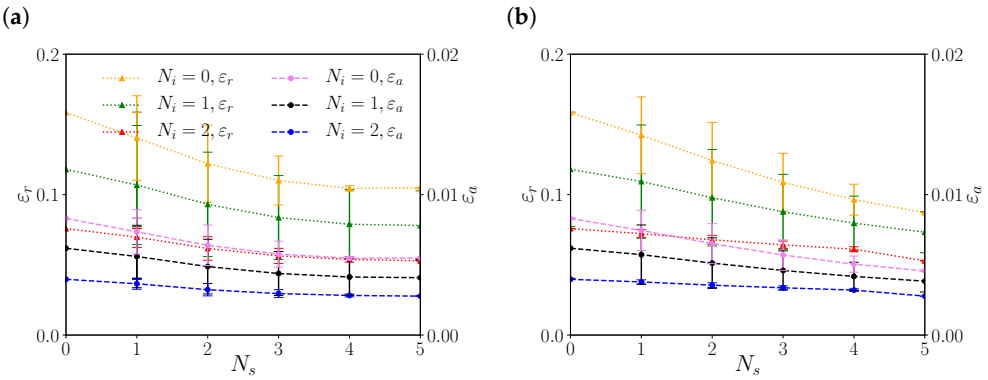

Figure A8. As in Figure 12, but for the heterogeneous neighbourhood and an easterly wind. (**a**) u_x; (**b**) u_y. $N_i = 0, \varepsilon_r$ are represented by yellow dotted lines;$N_i = 0, \varepsilon_a$ are represented by pink dashed lines; $N_i = 1, \varepsilon_r$ are represented by greed dotted lines; $N_i = 1, \varepsilon_a$ are represented by black dashed lines; $N_i = 2, \varepsilon_r$ are represented by red dotted lines; $N_i = 2, \varepsilon_a$ are represented by blue dashed lines;

Appendix F. Errors for the Different Computational Domains

Table A6. Absolute and relative errors for the deep canyon. $\varepsilon_a, \varepsilon_r$ are averaged over the whole canyon; $\varepsilon'_a, \varepsilon'_r$ exclude the bottom log layer.

		0°	**30°**	**45°**	**60°**	**90°**
u_x	ε_a	0.0042	0.0033	0.0038	0.0061	0.027
	ε'_a	0.0044	0.0034	0.0039	0.0062	0.028
	ε_r	0.48	0.35	0.32	0.42	0.66
	ε'_r	0.47	0.35	0.32	0.42	0.66
u_y	ε_a	0.019	0.010	0.0041	0.008	0.028
	ε'_a	0.019	0.010	0.0035	0.008	0.029
	ε_r	0.41	0.15	0.056	0.10	0.53
	ε'_r	0.39	0.13	0.05	0.10	0.54

Table A7. Absolute and relative errors for the homogeneous neighbourhood (Whampoa) and the optimal arrangement of vortex sheets ($\Omega^{best\,x}$ for u_x and $\Omega^{best\,y}$ for u_y; Equations (9a) and (10a)).

			0°	**30°**	**45°**	**60°**	**90°**	**Average**
Whampoa	u_x	ε_a	0.024	0.024	0.025	0.025	0.043	0.028
		ε_r	0.280	0.260	0.252	0.240	0.308	0.268
	u_y	ε_a	0.065	0.012	0.013	0.019	0.027	0.027
		ε_r	0.529	0.110	0.112	0.189	0.291	0.246

Table A8. Absolute and relative errors for the heterogeneous neighbourhood (Central) and the optimal vortex set, Equation (11).

			$D_{\mathbf{whole}}$, **W**	$D_{\Re^{i1}}$, **W**	$D_{\Re^{i2}}$, **W**	$D_{\mathbf{whole}}$, **E**	$D_{\Re^{i1}}$, **E**	$D_{\Re^{i2}}$, **E**
Central	u_x	ε_a	0.003	0.012	0.008	0.009	0.011	0.022
		ε_r	0.052	0.209	0.203	0.163	0.201	0.342
	u_y	ε_a	0.003	0.009	0.016	0.009	0.013	0.017
		ε_r	0.059	0.165	0.324	0.161	0.239	0.274

References

1. Richards, P.J.; Hoxey, R.P. Appropriate boundary conditions for computational wind engineering models using the k-ϵ turbulence model. *J. Wind. Eng. Ind. Aerodyn.* **1993**, *46–47*, 145–153. [CrossRef]
2. Richards, P.J.; Norris, S.E. Appropriate boundary conditions for computational wind engineering models revisited. *J. Wind. Eng. Ind. Aerodyn.* **2011**, *99*, 257–266. [CrossRef]
3. Wang, K.; Stathopoulos, T. Exposure model for wind loading of buildings. *J. Wind. Eng. Ind. Aerodyn.* **2007**, *95*, 1511–1525. [CrossRef]
4. Stockie, J.M. The mathematics of atmospheric dispersion modeling. *SIAM Rev.* **2011**, *53*, 349–372. [CrossRef]
5. Berkowicz, R. OSPM-A parameterised street pollution model. *Environ. Monit. Assess.* **2000**, *65*, 323–331. [CrossRef]
6. Soulhac, L.; Salizzoni, P.; Cierco, F.X.; Perkins, R. The model SIRANE for atmospheric urban pollutant dispersion; part i, presentation of the model. *Atmos. Environ.* **2011**, *45*, 7379–7395. [CrossRef]
7. Chen, F.; Kusaka, H.; Bornstein, R.; Ching, J.; Grimmond, C.S.; Grossman-Clarke, S.; Loridan, T.; Manning, K.W.; Martilli, A.; Miao, S.; et al. The integrated WRF/urban modelling system: Development, evaluation, and applications to urban environmental problems. *Int. J. Climatol.* **2011**, *31*, 273–288. [CrossRef]
8. Foken, T.; Napo, C.J. *Micrometeorology*, 2nd ed.; Springer: Berlin, Germany, 2008.
9. Cionco, R.M. A mathematical model for air flow in a vegetative canopy. *J. Appl. Meteorol. Climatol.* **1965**, *4*, 517–522. [CrossRef]
10. Barlow, J.F. Progress in observing and modelling the urban boundary layer. *Urban Clim.* **2014**, *10*, 216–240. [CrossRef]
11. Macdonald, R.W. Modelling the mean velocity profile in the urban canopy layer. *Bound.-Layer Meteorol.* **2000**, *97*, 25–45. [CrossRef]
12. Zajic, D.; Fernando, H.J.; Brown, M.J.; Pardyjak, E.R. On flows in simulated urban canopies. *Environ. Fluid Mech.* **2015**, *15*, 275–303. [CrossRef]
13. Castro, I.P. Are urban-canopy velocity profiles exponential? *Bound.-Layer Meteorol.* **2017**, *164*, 337. [CrossRef]
14. Di Sabatino, S.; Solazzo, E.; Paradisi, P.; Britter, R. A simple model for spatially-averaged wind profiles within and above an urban canopy. *Bound.-Layer Meteorol.* **2008**, *127*, 131–151. [CrossRef]
15. Ho, Y.K.; Liu, C.H. A wind tunnel study of flows over idealised urban surfaces with roughness sublayer corrections. *Theor. Appl. Climatol.* **2016**, *130*, 305–320. [CrossRef]
16. Duan, G.; Ngan, K. Effects of time-dependent inflow perturbations on turbulent flow in a street canyon. *Bound.-Layer Meteorol.* **2018**, *167*, 257–284. [CrossRef]
17. Vita, G.; Salvadori, S.; Misul, D.A.; Hemida, H. Effects of inflow condition on rans and les predictions of the flow around a high-rise building. *Fluids* **2020**, *5*, 233. [CrossRef]
18. Furtak-Cole, E.; Ngan, K. Predicting mean velocity profiles inside urban canyons. *J. Wind. Eng. Ind. Aerodyn.* **2020**, *207*, 104280. [CrossRef]
19. Saffman, P.G. *Vortex Dynamics*; Cambridge University Press: Cambridge, UK, 1992.
20. Wu, J.Z.; Ma, H.Y.; Zhou, M.D. *Vorticity and Vortex Dynamics*; Springer: Berlin, Germany, 2007.
21. Ngan, K.; Lo, K.W. Revisiting the flow regimes for urban street canyons using the numerical Green's function. *Environ. Fluid Mech.* **2016**, *16*, 313–334. [CrossRef]
22. Wang, H.; Brimblecombe, P.; Ngan, K. Particulate matter inside and around elevated walkways. *Sci. Total Environ.* **2020**, *699*, 134256. [CrossRef]
23. Yao, L.; Liu, C.H.; Mo, Z.; Cheng, W.C.; Brasseur, G.P.; Chao, C.Y. Statistical analysis of the organized turbulence structure in the inertial and roughness sublayers over real urban area by building-resolved large-eddy simulation. *Build. Environ.* **2022**, *207*, 108464. [CrossRef]
24. Li, X.X.; Liu, C.H.; Leung, D.Y.; Lam, K.M. Recent progress in CFD modelling of wind field and pollutant transport in street canyons. *Atmos. Environ.* **2006**, *40*, 5640–5658. [CrossRef]
25. Lin, Y.; Hang, J.; Yang, H.; Chen, L.; Chen, G.; Ling, H.; Sandberg, M.; Claesson, L.; Lam, C.K. Investigation of the Reynolds number independence of cavity flow in 2d street canyons by wind tunnel experiments and numerical simulations. *Build. Environ.* **2021**, *201*, 107965. [CrossRef]
26. Aboelata, A.; Sodoudi, S. Evaluating urban vegetation scenarios to mitigate urban heat island and reduce buildings' energy in dense built-up areas in Cairo. *Build. Environ.* **2019**, *166*, 106407. [CrossRef]
27. Ulpiani, G. On the linkage between urban heat island and urban pollution island: Three-decade literature review towards a conceptual framework. *Sci. Total Environ.* **2021**, *751*, 141727. [CrossRef] [PubMed]
28. Fan, Y.; Hunt, J.; Wang, Q.; Yin, S.; Li, Y. Water tank modelling of variations in inversion breakup over a circular city. *Build. Environ.* **2019**, *164*, 106342. [CrossRef]
29. Zhou, X.; Ying, A.; Cong, B.; Kikumoto, H.; Ooka, R.; Kang, L.; Hu, H. Large eddy simulation of the effect of unstable thermal stratification on airflow and pollutant dispersion around a rectangular building. *J. Wind. Eng. Ind. Aerodyn.* **2021**, *211*, 104526. [CrossRef]
30. Pullin, D.I. Contour dynamics methods. *Annu. Rev. Fluid Mech.* **1992**, *24*, 89–115. [CrossRef]
31. Flierl, G.R. Isolated eddy models in geophysics. *Annu. Rev. Fluid Mech.* **1987**, *19*, 493–550. [CrossRef]
32. Ngan, K.; Lo, K.W. Linear error dynamics for turbulent flow in urban street canyons. *J. Appl. Meteorol. Climatol.* **2017**, *56*, 1195–1208. [CrossRef]

33. Louka, P.; Belcher, S.E.; Harrison, R.G. Coupling between air flow in streets and the well-developed boundary layer aloft. *Atmos. Environ.* **2000**, *34*, 2613–2621. [CrossRef]
34. Guillas, S.; Glover, N.; Malki-Epshtein, L. Bayesian calibration of the constants of the k–ϵ turbulence model for a CFD model of street canyon flow. *Comput. Methods Appl. Mech. Eng.* **2014**, 279, 536–553. [CrossRef]
35. Weerasuriya, A.U.; Zhang, X.; Lu, B.; Tse, K.T.; Liu, C.H. Optimizing lift-up design to maximize pedestrian wind and thermal comfort in hot-calm and cold-windy climates. *Sustain. Cities Soc.* **2020**, *58*, 102146. [CrossRef]
36. Weerasuriya, A.U.; Zhang, X.; Lu, B.; Tse, K.T.; Liu, C.H. A Gaussian process-based emulator for modeling pedestrian-level wind field. *Build. Environ.* **2021**, *188*, 107500. [CrossRef]
37. Pope, S.B. *Turbulent Flows*; Cambridge University Press: Cambridge, UK, 2000.
38. Weller, H.G.; Tabor, G.; Jasak, H.; Fureby, C. A tensorial approach to computational continuum mechanics using object-oriented techniques. *Comput. Phys.* **1998**, *12*, 620–631. [CrossRef]
39. Darwish, M.; Moukalled, F. *The Finite Volume Method in Computational Fluid Dynamics*; Springer: Berlin, Germany, 2016.
40. Shur, M.L.; Spalart, P.R.; Strelets, M.K.; Travin, A.K. A hybrid RANS-LES approach with delayed-DES and wall-modelled LES capabilities. *Int. J. Heat Fluid Flow* **2008**, *29*, 1638–1649. [CrossRef]
41. Tominaga, Y.; Stathopoulos, T. CFD modeling of pollution dispersion in a street canyon: Comparison between LES and RANS. *J. Wind Eng. Ind. Aerodyn.* **2011**, *99*, 340–348. [CrossRef]
42. Spalding, D.B. A single formula for the law of the wall. *Appl. Mech.* **1961**, *28*, 455. [CrossRef]
43. Maronga, B.; Gryschka, M.; Heinze, R.; Hoffmann, F.; Kanani-Sühring, F.; Keck, M.; Ketelsen, K.; Letzel, M.O.; Sühring, M.; Raasch, S. The parallelized large-eddy simulation model (PALM) version 4.0 for atmospheric and oceanic flows: Model formulation, recent developments, and future perspectives. *Geosci. Model Dev.* **2015**, *8*, 2515–2551. [CrossRef]
44. Moeng, C.H.; Wyngaard, J.C. Spectral analysis of large-eddy simulations of the convective boundary layer. *J. Atmos. Sci.* **1988**, *45*, 3573–3587. [CrossRef]
45. Saiki, E.M.; Moeng, C.H.; Sullivan, P.P. Large-eddy simulation of the stably stratified planetary boundary layer. *Bound.-Layer Meteorol.* **2000**, *95*, 1–30. [CrossRef]
46. Castillo, M.C.; Inagaki, A.; Kanda, M. The effects of inner-and outer-layer turbulence in a convective boundary layer on the near-neutral inertial sublayer over an urban-like surface. *Bound.-Layer Meteorol.* **2011**, *140*, 453–469. [CrossRef]
47. Inagaki, A.; Castillo, M.C.; Yamashita, Y.; Kanda, M.; Takimoto, H. Large-eddy simulation of coherent flow structures within a cubical canopy. *Bound.-Layer Meteorol.* **2012**, *142*, 207–222. [CrossRef]
48. Han, B.S.; Baik, J.J.; Park, S.B.; Kwak, K.H. Large-eddy simulations of reactive pollutant dispersion in the convective boundary layer over flat and urban-like surfaces. *Bound.-Layer Meteorol.* **2019**, *172*, 271–289. [CrossRef]
49. Gronemeier, T.; Raasch, S.; Ng, E. Effects of unstable stratification on ventilation in Hong Kong. *Atmosphere* **2017**, *8*, 168. [CrossRef]
50. Wang, H.; Ngan, K. Effects of inhomogeneous ground-level pollutant sources under different wind directions. *Environ. Pollut.* **2021**, *289*, 117903. [CrossRef] [PubMed]
51. Kim, J.J.; Baik, J.J. Urban street-canyon flows with bottom heating. *Atmos. Environ.* **2001**, *35*, 3395–3404. [CrossRef]
52. Cheng, W.C.; Liu, C.H. Large-eddy simulation of flow and pollutant transports in and above two-dimensional idealized street canyons. *Bound.- Layer Meteorol.* **2011**, *139*, 411–437. [CrossRef]
53. Li, X.X.; Britter, R.; Norford, L.K. Effect of stable stratification on dispersion within urban street canyons: A large-eddy simulation. *Atmos. Environ.* **2016**, *144*, 47–59. [CrossRef]
54. Lawson, R.E., Jr.; Lee, R.L. Mean flow and turbulence measurements around a 2-D array of buildings in a wind tunnel. In Proceedings of the 11th Joint AMS/AWMA Conference on the Applications of Air Pollution Meteorology, Long Beach, CA, USA, 9 January 2000.
55. Duan, G.; Takemi, T. Predicting urban surface roughness aerodynamic parameters using random forest. *J. Appl. Meteorol. Climatol.* **2021**, *60*, 999–1018. [CrossRef]
56. Kwak, K.H.; Baik, J.J.; Ryu, Y.H.; Lee, S.H. Urban air quality simulation in a high-rise building area using a CFD model coupled with mesoscale meteorological and chemistry-transport models. *Atmos. Environ.* **2015**, *100*, 167–177. [CrossRef]
57. Chang, J.C.; Hanna, S.R. Air quality model performance evaluation. *Meteorol. Atmos. Phys.* **2004**, *87*, 167–196. [CrossRef]
58. Uehara, K.; Murakami, S.; Oikawa, S.; Wakamatsu, S. Wind tunnel experiments on how thermal stratification affects flow in and above urban street canyons. *Atmos. Environ.* **2000**, *34*, 1553–1562. [CrossRef]
59. Oke, T.R. Street design and urban canopy layer climate. *Energy Build.* **1988**, *11*, 103–113. [CrossRef]
60. Hunter, L.J.; Watson, I.D.; Johnson, G.T. Modelling air flow regimes in urban canyons. *Energy Build.* **1990**, *15*, 315–324. [CrossRef]
61. He, L.; Hang, J.; Wang, X.; Lin, B.; Li, X.; Lan, G. Numerical investigations of flow and passive pollutant exposure in high-rise deep street canyons with various street aspect ratios and viaduct settings. *Sci. Total Environ.* **2017**, *584*, 189–206. [CrossRef]
62. Chew, L.W.; Aliabadi, A.A.; Norford, L.K. Flows across high aspect ratio street canyons: Reynolds number independence revisited. *Environ. Fluid Mech.* **2018**, *18*, 1275–1291. [CrossRef]
63. Addepalli, B.; Pardyjak, E.R. Investigation of the flow structure in step-up street canyons—Mean flow and turbulence statistics. *Bound.-Layer Meteorol.* **2013**, *148*, 133–155. [CrossRef]
64. Addepalli, B.; Pardyjak, E.R. A study of flow fields in step-down street canyons. *Environ. Fluid Mech.* **2015**, *15*, 439–481. [CrossRef]

65. Nazarian, N.; Kleissl, J. Realistic solar heating in urban areas: Air exchange and street-canyon ventilation. *Build. Environ.* **2016**, *95*, 75–93. [CrossRef]
66. Wood, C.R.; Järvi, L.; Kouznetsov, R.D.; Nordbo, A.; Joffre, S.; Drebs, A.; Vihma, T.; Hirsikko, A.; Suomi, I.; Fortelius, C.; et al. An overview of the urban boundary layer atmosphere network in Helsinki. *Bull. Am. Meteorol. Soc.* **2013**, *94*, 1675–1690. [CrossRef]
67. Tian, G.; Conan, B.; Calmet, I. Turbulence-kinetic-energy budget in the urban-like boundary layer using large-eddy simulation. *Bound.-Layer Meteorol.* **2020**, *178*, 201–223. [CrossRef]
68. Duan, G.; Ngan, K. Sensitivity of turbulent flow around a 3-d building array to urban boundary-layer stability. *J. Wind. Eng. Ind. Aerodyn.* **2019**, *193*, 103958. [CrossRef]
69. Lo, K.W.; Ngan, K. Characterising urban ventilation and exposure using Lagrangian particles. *J. Appl. Meteorol. Climatol.* **2017**, *56*, 1177–1194. [CrossRef]
70. Chatzimichailidis, A.E.; Argyropoulos, C.D.; Assael, M.J.; Kakosimos, K.E. Qualitative and quantitative investigation of multiple large eddy simulation aspects for pollutant dispersion in street canyons using openfoam. *Atmosphere* **2019**, *10*, 17. [CrossRef]